The WiggleZ Dark Energy Survey: high-resolution kinematics of luminous star-forming galaxies

Emily Wisnioski,[1]* Karl Glazebrook,[1] Chris Blake,[1] Ted Wyder,[2] Chris Martin,[2] Gregory B. Poole,[1] Rob Sharp,[3] Warrick Couch,[1] Glenn G. Kacprzak,[1] Sarah Brough,[4] Matthew Colless,[4] Carlos Contreras,[1] Scott Croom,[5] Darren Croton,[1] Tamara Davis,[6] Michael J. Drinkwater,[6] Karl Forster,[2] David G. Gilbank,[7] Michael Gladders,[8] Ben Jelliffe,[5] Russell J. Jurek,[9] I-hui Li,[1] Barry Madore,[10] Kevin Pimbblet,[11] Michael Pracy,[1,3] David Woods[12] and H. K. C. Yee[13]

[1]*Centre for Astrophysics and Supercomputing, Swinburne University of Technology, PO Box 218, Hawthorn, VIC 3122, Australia*
[2]*California Institute of Technology, MC 405-47, 1200 East California Boulevard, Pasadena, CA 91125, USA*
[3]*Research School of Astronomy & Astrophysics, Australian National University, Weston Creek, ACT 2600, Australia*
[4]*Australian Astronomical Observatory, PO Box 296, Epping, NSW 2121, Australia*
[5]*School of Physics, University of Sydney, NSW 2006, Australia*
[6]*Department of Physics, University of Queensland, Brisbane, QLD 4072, Australia*
[7]*Department of Physics and Astronomy, University of Waterloo, Waterloo, ON N2L 3G1, Canada*
[8]*Department of Astronomy and Astrophysics, The University of Chicago, 5640 S. Ellis Ave, Chicago, IL 60637, USA*
[9]*CSIRO Astronomy & Space Sciences, Australia Telescope National Facility, Epping, NSW 1710, Australia*
[10]*Observatories of the Carnegie Institute of Washington, 813 Santa Barbara St., Pasadena, CA 91101, USA*
[11]*School of Physics, Monash University, Clayton, VIC 3800, Australia*
[12]*Department of Physics & Astronomy, University of British Columbia, 6224 Agricultural Road, Vancouver, BC V6T 1Z1, Canada*
[13]*Department of Astronomy & Astrophysics, University of Toronto, 50 St. George St., Toronto, ON M5S 3H4, Canada*

ABSTRACT

We report evidence of ordered orbital motion in luminous star-forming galaxies at $z \sim 1.3$. We present integral field spectroscopy (IFS) observations, performed with the OH Suppressing InfraRed Imaging Spectrograph (OSIRIS) system, assisted by laser guide star adaptive optics on the Keck telescope, of 13 star-forming galaxies selected from the WiggleZ Dark Energy Survey. Selected via ultraviolet and [O II] emission, the large volume of the WiggleZ survey allows the selection of sources which have comparable intrinsic luminosity and stellar mass to IFS samples at $z > 2$. Multiple 1–2 kpc size subcomponents of emission, or 'clumps', are detected within the Hα spatial emission which extends over 6–10 kpc in four galaxies, resolved compact emission ($r < 3$ kpc) is detected in five galaxies and extended regions of Hα emission are observed in the remaining four galaxies. We discuss these data in the context of different snapshots in a merger sequence and/or the evolutionary stages of coalescence of star-forming regions in an unstable disc. We find evidence of ordered orbital motion in galaxies as expected from disc models and the highest values of velocity dispersion ($\sigma > 100 \, \mathrm{km \, s^{-1}}$) in the most compact sources. This unique data set reveals that the most luminous star-forming galaxies at $z > 1$ are gaseous unstable discs indicating that a different mode of star formation could be feeding gas to galaxies at $z > 1$, and lending support to theories of cold dense gas flows from the intergalactic medium.

Key words: galaxies: evolution – galaxies: formation – galaxies: high-redshift – galaxies: kinematics and dynamics.

1 INTRODUCTION

An open question remains regarding the accretion of gas and build up of stars in massive galaxies at the peak epoch of cosmic star

*E-mail: ewisnios@astro.swin.edu.au

formation. The traditional theories of isolated disc formation resulting from gas accretion from the halo (Eggen, Lynden-Bell & Sandage 1962) have been challenged by recent observations and theories at high redshift. In new models of disc formation at high redshift, cooling flows supply gas directly to the centres of galaxies (Kereš et al. 2005; Dekel et al. 2009a). Direct observations of the gas motions in galaxies are crucial to test these new models and ultimately to disentangle how galaxies form at high redshift.

Morphological studies made possible by Hubble Advanced Camera for Surveys (ACS), Wide Field and Planetary Camera (WFPC) and other deep imagers have provided the first clues to the processes governing high-redshift galaxy formation. High-redshift galaxies exhibit different morphologies to local galaxies, with higher fractions of both compact and irregular galaxies (Glazebrook et al. 1995; Abraham et al. 1996). This deviation from the Hubble sequence indicates that different mechanisms may be driving star formation and galaxy evolution at earlier cosmic times. Initial interpretations of the complex structures seen in the *Hubble Ultra Deep Field* (HUDF) favour higher rates of major mergers, a natural consequence of hierarchical merging models in a Λ cold dark matter (ΛCDM) Universe (e.g. Conselice et al. 2003; Lotz et al. 2006; Overzier et al. 2008; Engel et al. 2010). Yet, despite large dense regions in these galaxies, observations of their stellar populations reveal galactic properties reminiscent of local disc galaxies (Elmegreen & Elmegreen 2005). In this case the large dense regions or 'clumps' of star formation may be related to H II regions found in spiral galaxies but of much larger size (Jones et al. 2010; Swinbank et al. 2010). Models have been developed to explain the clumpy structures in discs and their evolution into galactic structures seen at $z = 0$ (e.g. Noguchi 1999; Immeli et al. 2004a; Bournaud, Elmegreen & Elmegreen 2007; Elmegreen, Bournaud & Elmegreen 2008, hereafter EBE08). In these models, turbulent gas collapses from Jeans instabilities resulting in massive star clusters that, on a time-scale of 1 Gyr, coalesce to the centre of the galaxy to form a pseudo-bulge.

Morphological studies alone do not provide enough information to distinguish between the two kinematically distinct formation theories of merging and isolated disc formation at these redshifts. Given the complex structure of the galaxies it is difficult to derive the major axis for slit positioning making spectroscopic observations less effective in discerning rotation signatures (e.g. Erb et al. 2004, 2006). Spatially resolved spectroscopy is therefore essential for disentangling kinematics and star formation histories of galaxies at high redshift.

The past 5 years have seen a great number of integral field spectroscopy (IFS) studies of the nebular emission line, Hα, in $z > 2$ star-forming galaxies (e.g. Genzel et al. 2006, 2008; Wright et al. 2007, 2009; Nesvadba et al. 2008; Epinat et al. 2009; Förster Schreiber et al. 2009; Law et al. 2009). These redshifts are favoured due to the large number of Lyman-break galaxies (LBGs) and submillimetre galaxies (SMGs) being discovered by methods tailored for high redshift as well as the accessibility of Hα in the near-infrared (NIR).

The main focus of these studies is the classification of galaxies kinematically to define clear observational distinctions between discs and interacting systems. Mergers observed with integral field units (IFUs; Nesvadba et al. 2008; Wright et al. 2009) often show clear kinematic steps across one resolution element, indicating separation between two kinematically separate systems, whilst discs are identified by rotational signatures found in both velocity and velocity dispersion maps. A growing number of massive discs have been found with IFS at $z > 2$ which are well fit by disc models and which have Toomre parameters of $Q > 1$ indicating stable rotationally supported discs, lending observational support to theories of rapid accretion of cold gas and secular disc evolution at high redshift (Genzel et al. 2008; Epinat et al. 2009; Lemoine-Busserolle & Lamareille 2010).

However, classifying galaxies in these two distinct groups is an oversimplification. Many of the samples present a variety of kinematic types including dispersion-dominated systems, stable discs, unstable discs, minor mergers, mergers and merger remnants. Law et al. (2009) present a sample of lower mass ($M_{*,\mathrm{avg}} = 2 \times 10^{10}\,\mathrm{M_\odot}$) galaxies with kinematics dominated by dispersion. Their results can be interpreted as merger remnants, however, they also caution that this is statistically unlikely and find that the kinematic classifications are a crude oversimplification. They argue that their galaxies are observed at a range of times during their formation, and that their kinematic signatures are a result of how they acquire their gas. Despite the different kinematic interpretations, all high-redshift IFS samples show high dispersions ($\sigma \gtrsim 90\,\mathrm{km\,s^{-1}}$) with many (20–100 per cent) systems showing no ordered rotation making classifications uncertain (e.g. Genzel et al. 2008; Förster Schreiber et al. 2009; Law et al. 2009; Wright et al. 2009).

With observation times ranging from 2000 to 40 000 s, it is only possible to follow up a small fraction of the brightest galaxies at these redshifts. To supplement high-redshift kinematic results other studies target lensed galaxies magnified in both size and flux, allowing the study of sub-L_* galaxies (Jones et al. 2010). Using this strategy, IFUs have probed all the way out to $z = 4.9$ (Swinbank et al. 2009) and have targeted strongly lensed galaxies at $z = 1.4$–3.1 (Stark et al. 2008; Jones et al. 2010; Yuan et al. 2011). With galaxy magnification individual clumps have been resolved with diameters of $\sim$500 pc which will be essential in testing the models of clumpy disc formation (Swinbank et al. 2009, 2010; Jones et al. 2010). However, more kinematically resolved clumps are needed than are available from current studies ($\sim$20 at $z > 1$) in order to rigorously compare with models.

Despite great advantages, lensed studies require strong lenses with confirmed redshifts which can be observationally expensive in addition to requiring reliable lensing models and reconstruction. Furthermore, rather than bridge the gap between the $z \sim 2$–3 results and local galaxies, the majority of current lensing studies push out to higher redshifts.

In order to correctly interpret IFS data at high redshift it is critical to utilize low-redshift IFS results. By comparing directly to these data and by artificially redshifting them out to $z > 1$ a better understanding of different kinematic signatures in the high-redshift data can be reached. Recent efforts by Epinat et al. (2010) have supplied a sizable sample of Fabry–Perot 3D data of Hα emission in 153 nearby isolated galaxies. Disc models are fit to the local population and to the same galaxies artificially redshifted to $z = 1.7$, providing guidance in the best disc models to use to fit to high-redshift kinematic results. Green et al. (2010) and Rodríguez-Zaurín et al. (2011) also provide local comparison samples for Hα velocity dispersion and morphology. Properties observed locally at parsec to kiloparsec resolution are crucial for the interpretation of high-redshift IFU observations.

Connecting the $z < 0.2$ and >1.5 results is a relative dearth of IFS studies at $z \sim 1$. At this redshift, galaxies are at the tail end of the epoch of mass assembly but at more accessible distances for current instrumentation where $(1 + z)^4$ surface brightness dimming is less severe. Yet suitable galaxies for such studies are rare as once the main epoch of massive galaxy formation is over at $z \sim 2$, the abundance of galaxies with high star formation rates (SFRs) falls rapidly. They are difficult to select with the Lyman-break technique at $z \sim 1$ as the drop in emission blueward of 912 Å cannot be

detected with the low sensitivity and resolution of ultraviolet (UV) instruments. These galaxies can, however, be found in very large high-redshift surveys, such as the WiggleZ Dark Energy Survey. The WiggleZ survey contains a rare population of UV-luminous galaxies out to $z = 1.5$ with SFRs (from nebular emission) of $\sim 100 \, \mathrm{M}_\odot \, \mathrm{yr}^{-1}$. These galaxies may be the link needed to bridge the gap between observations of local luminous galaxies, and LBGs and SMGs found at higher redshift. In this paper, we present IFS of the Hα emission line in 13 star-forming galaxies from the WiggleZ Dark Energy Survey at $z \sim 1.3$.

In this paper, we present 13 galaxies and their physical properties. In Section 2 we describe our sample selection, observational technique and data reduction methods. In Section 3 we discuss the properties of the galaxies, in particular we describe the morphological and kinematic properties. In Sections 3.6 and 3.7 we discuss the methods of disc fitting and surface brightness profile fitting analysis. The individual and global properties of the 13 systems described in Section 3 are analysed in Section 4 in the context of theories of galaxy formation at high redshift and the implications for the mechanism triggering massive rates of star formation. We conclude with a summary of our results and interpretations in Section 5, giving a brief list of the key points presented in this paper. The properties of the 13 individual galaxies are described individually in Appendix A.

A standard ΛCDM cosmology of $\Omega_\mathrm{m} = 0.3$, $\Omega_\Lambda = 0.7$, $h = 0.7$ is adopted throughout this paper (e.g. Komatsu et al. 2011). In this cosmology, at redshift $z = 1.3$, 1 arcsec corresponds to 8.38 kpc.

2 OBSERVATIONS

2.1 Target selection

Our sample of 13 galaxies was selected from the WiggleZ Dark Energy Survey (Drinkwater et al. 2010). WiggleZ is a UV-selected survey of 238 770 unique emission-line galaxies in the redshift range $0 < z < 1.5$, observed over 245 nights with the AAOmega spectrograph (Sharp et al. 2006) on the 3.9-m Anglo-Australian Telescope (AAT). The primary aim of the survey is to precisely measure the scale of baryon acoustic oscillations imprinted on the spatial distribution of these galaxies at look-back times of 4–8 Gyr (Blake et al. 2011). The survey samples a total volume of $\sim 1 \, \mathrm{Gpc}^3$ over 816 deg^2 of sky across seven fields, with an average target density of 350 galaxies deg^{-2}. Photometric data used in target selection for the WiggleZ survey are from the *Galaxy Evolution Explorer* (*GALEX*) satellite (Martin et al. 2005), the Fourth Data Release of the Sloan Digital Sky Survey (SDSS; Adelman-McCarthy et al. 2006) in the northern galactic region and the Canada–France–Hawaii Telescope second Red-sequence Cluster Survey (RCS2; Gilbank et al. 2011) in the southern galactic region.

Whilst the WiggleZ galaxy redshift distribution peaks at $z \sim 0.6$ a long thin tail of high-redshift galaxies reaches to $z = 1.5$. These high-redshift galaxies are identified by strong [O II] emission lines, with the [O II] doublet marginally resolved, and have SFRs of $>50 \, \mathrm{M}_\odot \, \mathrm{yr}^{-1}$.

Galaxies selected for this study were drawn from the WiggleZ survey subject to a variety of criteria. Primary selection required (1) redshifts of $1.2 < z < 1.5$, where the [O II] emission line falls between OH sky residuals at ~ 8000–$10\,000$ Å, (2) [O II] emission exceeding $50 \times 10^{-15} \, \mathrm{erg} \, \mathrm{s}^{-1} \, \mathrm{cm}^{-2}$. We found ~ 300 targets in the WiggleZ survey that satisfied the aforementioned criteria. To reduce contamination from active galactic nuclei (AGN), starbursts were preferentially selected by (3) omitting galaxies with [Mg II] emis-

sion visible in the WiggleZ spectrum which may be indicative of AGN activity (Grandi & Phillips 1979). With the additional criteria the number of targets was reduced to ~ 100 galaxies. Finally, for IFU observations with laser guide star adaptive optics (LGSAO), a suitable tip-tilt star is required to correct aberrations in the wavefront. We require a star with apparent r-band magnitude $m_r \lesssim 17$ with an angular separation <60 arcsec from the science target for optimal acquisition. This last criteria reduced our final target sample to ~ 50 targets.

2.2 OSIRIS observations

Out of the possible targets, spanning across seven fields, we observed 17 star-forming galaxies with the OH Suppressing InfraRed Imaging Spectrograph (OSIRIS; Larkin et al. 2006) with the Keck II LGSAO system (van Dam et al. 2006; Wizinowich et al. 2006). These 17 targets were prioritized for having the brightest tip-tilt stars with shortest separation, and for which [O II] and Hα fall fortuitously in clean sky regions. OSIRIS is a lenslet array spectrograph with a 2048×2048 Hawaii-2 detector and spectral resolution $R \sim 3600$. Observations were performed in 2008 September, 2009 May, September and December and 2010 March. The filters *Hn1*, *Hn2* and *Hn3* were used with central wavelengths of 1.500, 1.569 and 1.635 μm, respectively, in the 0.05 arcsec pixel scale. The full width at half-maximum (FWHM) of the tip-tilt stars ranged from one and a half to two pixels, 0.062–0.1 arcsec, with an average Strehl of 30 per cent estimated from the tip-tilt stars. Seeing ranged from 0.4 to 1.4 arcsec. The galaxies observed on these nights are listed in Table 1.

The standard observing procedure was as follows. We first acquired the tip-tilt star and applied the optimal position angle of OSIRIS to position the star within the unvignetted field-of-view of the LGSAO system. Short, 60 s, integrations were taken on the star for calculations of the point spread function (PSF) and to centre the star in the field. A blind offset was then applied to the telescope to acquire the target. The WiggleZ survey selected targets from SDSS and RCS2 which follow different astrometry systems (Drinkwater et al. 2010). In calculating offsets from the reference star to the target, Two Micron All Sky Survey (2MASS; Skrutskie et al. 2006) and USNO-B (Monet et al. 2003) coordinates were used for SDSS and RCS2 galaxies, respectively. The typical science observing sequence was to expose on target for 900 s in each of two nod positions, A and B, separated by 1.6 arcsec on the detector. If Hα emission was detected in the difference of the first two exposures, we continued to expose on the galaxy for ~ 1–2 h as necessary to achieve a high signal-to-noise ratio detection. Multiple A and B positions were dithered by 0.05 arcsec around the base positions in each exposure to remove bad pixels and cosmic ray contamination. Of the 17 observed targets, Hα was detected in the spectra of 15 targets. The two non-detections were a result of the [O III]λ5007 emission line being misidentified as [O II]λ3727 in the WiggleZ spectrum. Of the 15 detected targets, observations for two galaxies are unusable for scientific reduction due to poor adaptive optics (AO) correction as a result of stray light on the low bandwidth wavefront sensor. The Hα luminosities of the final 13 galaxies are shown in Fig. 1 with [O II] luminosities of all possible targets indicated by the small grey filled circles.

Data reduction was completed with the OSIRIS data reduction pipeline versions 2.2 and 2.3 and custom IDL routines developed for faint emission-line spectra. The pipeline removes cross-talk, detector glitches and cosmic rays before it mosaics individual exposures and assembles a reduced data cube with two spatial and

Table 1. OSIRIS observations of WiggleZ galaxies.

WiggleZ ID	ID	RA (J2000.0)	Dec. (J2000.0)	z^a	Obs. date	$t_{exp.}$ (s)	Exp. seq.	Filter	Scale (mas)
			Detections						
R03J032450240−13550943	WK0912_13R	03:24:50.240	−13:55:09.429	1.288	2009/12	3600	4 × 900	*Hn1*	50
S15J145355248−00320351	WK1002_61S	14:53:55.247	−00:32:03.501	1.305	2010/02	5400	6 × 900	*Hn1*	50
R01J005822757−03034040	WK0909_02R	00:58:22.757	−03:03:40.400	1.362	2009/09	5400	9 × 600	*Hn2*	50
R03J032206214−15443471	WK0909_06R	03:22:06.214	−15:44:34.711	1.461	2009/09	8100	9 × 900	*Hn3*	50
S15J144102444+05480354	WK0905_22S	14:41:02.443	05:48:03.540	1.282	2009/05	3600	4 × 900	*Hn1*	50
R00J232217805−05473356	WK0912_01R	23:22:17.805	−05:47:33.560	1.297	2009/12	3600	4 × 900	*Hn1*	50
S09J091517481+00033557	WK1002_41S	09:15:17.483	00:03:35.570	1.334	2010/02	7200	8 × 900	*Hn1*	50
S00J233338383−01040629	WK0809_02S	23:33:38.386	−01:04:06.290	1.452	2008/09	5400	6 × 900	*Hn3*	50
S11J101757445−00244002	WK1002_14S	10:17:57.444	−00:24:40.020	1.305	2010/02	5400	6 × 900	*Hn1*	50
S15J142538641+00483135	WK1002_18S	14:25:38.639	00:48:31.350	1.305	2010/02	2700	3 × 900	*Hn1*	50
S09J090933680+01074587	WK1002_46S	09:09:33.680	01:07:45.870	1.308	2010/02	3000	5 × 600	*Hn1*	50
S11J110405504+01185565	WK1002_52S	11:04:05.504	01:18:55.650	1.320	2010/02	7200	8 × 900	*Hn1*	50
S09J090312056−00273273	WK0912_16R	09:03:12.056	−00:27:32.730	1.327	2009/12	8100	9 × 900	*Hn1*	50
R00J233618953−10580749^b	WK0809_05R	23:36:18.955	−10:58:07.321	1.402	2008/09	2700	3 × 900	*Hn2*	100
R00J232248993−12151943^b	WK0809_04R	23:22:48.992	−12:15:19.439	1.455	2008/09	2700	3 × 900	*Hn3*	50
			Misidentifications						
R22J214700239+01333423	WK0809_01R	21:47:00.239	01:33:34.230	1.466	2008/09	3600	4 × 900	*Hn3*	50
S00J234420801−09322580	WK0809_03S	23:44:20.801	−09:32:25.800	1.488	2008/09	2700	3 × 900	*Hn3*	50

^{a}WiggleZ Dark Energy Survey spectroscopic redshift.
^{b}Hα detected but observations unusable due to poor AO correction as a result of stray light on the low bandwidth wavefront sensor.
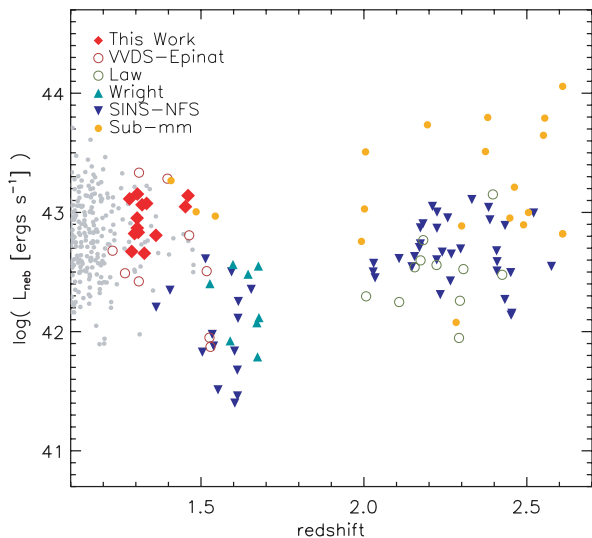

Figure 1. Nebular luminosity as a function of redshift for the largest high-redshift IFS surveys with the work presented here shown by the red diamonds. The grey points show the [O II] luminosity of other WiggleZ galaxies considered for this sample. The red circles show the sample from Epinat et al. (2009) taken from the VVDS and observed with SINFONI on the Very Large Telescope (VLT). The green circles show the sample from Law et al. (2009) observed with OSIRIS on Keck. The blue inverted triangles show the SINS sample from Förster Schreiber et al. (2009) observed with SINFONI, and the green triangles show the sample from Wright et al. (2009) observed with OSIRIS. The orange points are SMGs with measured Hα taken from Swinbank et al. (2004) and Takata et al. (2006).

one wavelength dimension. First-order sky subtraction was achieved by the spatial ABBA nodding on the sky. Further sky subtraction was applied using custom IDL routines which employ the sky subtraction methods of Davies (2007). Galaxies were flux calibrated

using telluric standard stars observed throughout the night. On average three telluric standards were observed each night.

2.3 Kinematic mapping

In order to create 2D spatial and kinematic maps of the Hα emission line, the sky-subtracted data cube was convolved with a Gaussian kernel with FWHM = 150 mas (200 mas in cases of low signal) to achieve a higher signal-to-noise ratio in each spaxel. A Gaussian profile was then fitted to the Hα emission in each spaxel of the cube with the wavelength, intensity and width as free parameters. Errors were calculated by adding in quadrature an estimation of the sky noise from the variance of the spectrum offset from the emission lines with the Poisson error of the photon counting statistics in the emission lines. Spaxels were masked from the Hα emission map and kinematic maps if the peak of the fitted Gaussian was less than one standard deviation above the median of the spectrum (corresponding to minimum signal-to-noise ratio of ∼2), or the width of the Gaussian was less than the resolving power of the instrument. For spaxels surviving these cuts a flux was calculated from the fitted Gaussian. The Hα flux images represent this array of fluxes. The integrated spectra, shown in Fig. 2, were created by summing all unmasked spaxels in the spatial directions. A Gaussian was fitted to the observed-frame integrated spectrum to obtain the total Hα flux and the systematic redshift, z_{sys}, given in Table 2. A velocity map was constructed for each galaxy using the velocity shifts of the emission line in each spaxel relative to z_{sys}. The velocity dispersion was measured in each spaxel from the rms of the fitted Gaussian line profile corrected for instrumental broadening. All kinematic maps are shown in Fig. 3.

2.4 NIRSPEC observations and data reduction

When the Keck LGSAO system was unavailable due to bad weather, technical faults or 'space events', observations of available targets
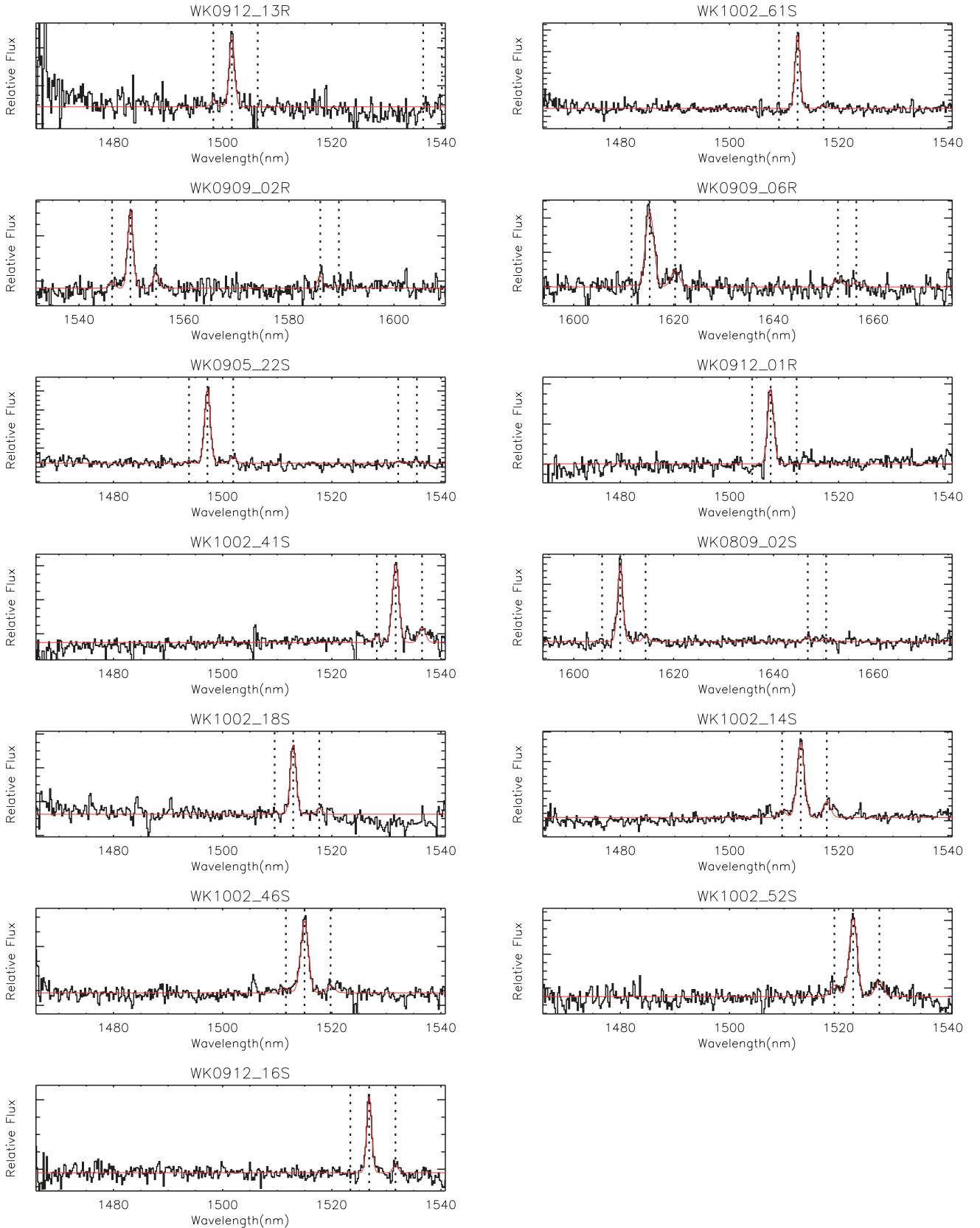
Figure 2. OSIRIS integrated spectra of each galaxy over all pixels satisfying the criteria outlined in Section 2. The vertical dotted lines denote the position of the redshifted locations of nebular emission lines: Hα, [N II]$\lambda\lambda$6548, 6584 and [S II]$\lambda\lambda$6716, 6731 at the systematic redshift. The solid red line is the best-fitting single Gaussian fits to each detected emission line.

Table 2. Emission-line properties.

WiggleZ ID	ID	$z_{\rm sys}^a$	$f_{\rm H\alpha}^b$	$f_{\rm [N\,II]}^b$	$L_{\rm H\alpha}$ $(10^{41}\,{\rm erg\,s^{-1}})$	$12 + \log({\rm O/H})$
R03J032450240−13550943	WK0912_13R	1.2873	48 ± 16.1	<8.4	46.8 ± 13.2	<8.47
S15J145355248−00320351	WK1002_61S	1.3039	81.5 ± 5.3	<9.4	81.9 ± 13.7	<8.37
R01J005822757−03034040	WK0909_02R	1.3616	41.5 ± 7.9	9.3 ± 4.4	46.4 ± 15.2	8.53 ± 0.29
R03J032206214−15443471	WK0909_06R	1.4602	94.9 ± 6.7	22.8 ± 3.7	126.2 ± 18.1	8.55 ± 0.1
S15J144102444+05480354	WK0905_22S	1.2810	105.4 ± 4.3	10.8 ± 2.3	101.4 ± 13.1	8.34 ± 0.12
R00J232217805−05473356	WK0912_01R	1.2960	57.3 ± 7.5	<6.4	56.7 ± 13.5	<8.36
S09J091517481+00033557	WK1002_41S	1.3330	64.9 ± 4.3	13.7 ± 2.4	68.9 ± 14.4	8.52 ± 0.1
S00J233338383−01040629	WK0809_02S	1.4521	74.7 ± 13.6	6.3 ± 7.3	98.0 ± 17.8	8.29 ± 0.68
S15J142538641+00483135	WK1002_18S	1.3044	58.0 ± 4.8	<7.6	58.4 ± 13.7	<8.4
S11J101757445−00244002	WK1002_14S	1.3048	92.8 ± 4.3	20.6 ± 2.4	93.5 ± 13.7	8.53 ± 0.07
S09J090933680+01074587	WK1003_46S	1.3074	50.0 ± 4.5	<5.6	50.6 ± 13.8	<8.36
S11J110405504+01185565	WK1003_52S	1.3191	86.1 ± 6.0	20.4 ± 3.4	89.0 ± 14.1	8.54 ± 0.1
S09J090312056−00273273	WK0912_16S	1.3260	38.6 ± 4.4	7.5 ± 2.4	40.5 ± 14.3	8.49 ± 0.19

[a]Systematic redshift measured from Gaussian fit to Hα emission in integrated spectrum.
[b]Emission line flux in units of $10^{-17}\,{\rm erg\,s^{-1}\,cm^{-2}}$.

were taken with the near-infrared echelle spectrograph (NIRSPEC; McLean et al. 1998) to measure the Hβ and [O III] emission line ratio. The ratios of emission lines from these observations, obtained for WK0905_22S, WK1002_18S, WK1002_52S, WK1002_61S, are used to constrain their AGN contamination as discussed in Section 3.4.

The NIRSPEC detector is a 1024 × 1024 ALADDIN-3 InSb detector with spectral resolution $R \sim 2000$. All observations were carried out in 2010 February with the 4 pixel slit (42 × 0.76 arcsec^2) in the *NIRSPEC-2* filter (1.089–1.293 μm). Seeing in K was 0.8 arcsec on average.

The typical observing sequence is as follows. To acquire a guide star, typically the star already selected for use with OSIRIS LGSAO system, short (∼10 s) images were taken with the NIRSPEC guider to centre the star at the central position on the slit. Once centred a blind offset was applied to the star position. Longer images were taken (2 × 20 s) at the target position. If the target was observed in these images it was centred on the slit by nudging the slit left and right in single pixel intervals. Once centred spectroscopic object exposures were taken with typical sequence of 2 × 600 s in each of two nod positions, A and B in the sequence ABBA. Occasional shifts of a few pixels were needed to keep the object on the slit throughout the object exposures. No continuum was detected and the ratio of [O III]λ5007/Hβλ4861 was calculated from the raw data.

2.5 IRIS2 observations

NIR imaging was obtained for nine out of 13 galaxies in the sample with the Infrared Imager and Spectrograph (IRIS2; Tinney et al. 2004) on the AAT. J and K_s bands, with central wavelengths $\lambda_c = 1.245$ and 2.1444 μm, respectively, were chosen in order to image the older stellar population of each galaxy to obtain robust estimates of stellar masses. The IRIS2 detector is a 1024 × 1024 Rockwell HAWAII-1 HgCdTe infrared detector, with a scale of 0.4487 arcsec pixel^{-1} and field of view of 7.7 arcmin^2. Observations were carried out during 2009 May, 2010 January and 2010 July. Seeing in K_s ranged between 0.9–2.5, 0.9–1.6 and 1.3–2.0 arcsec, respectively.

The typical J exposure sequence was a series of 15-s exposures totalling 1350 s on the target. The typical K_s exposure sequence was a series of 10-s exposures totalling 1350 s on target. Most galaxies

required two or three sequences in K_s in order to obtain a detection with a signal-to-noise ratio greater than 5. Because of the time-sensitive variation of the infrared night sky, we used a dithering strategy of successive observations with nine dithers per sequence with a maximum dither length of 20 arcsec.

Data reduction and mosaicking was carried out by data reduction pipeline ORAC-DR (Cavanagh et al. 2003). Each image was flattened with the other images closest in time and position in the dither pattern. The dithering script averaged out bad pixels on the detector and applied a nearest neighbour smoothing.

Magnitudes were calculated in the AB system using aperture photometry with a circular aperture of 4 arcsec with a concentric sky annulus. A zero-point was derived for each reduced mosaicked image by comparing the measured aperture counts with known 2MASS magnitudes for several stars in the image. The zero-point was then used to photometrically calibrate the image. On average, four uncrowded central stars with K-band magnitudes of $K \sim 15$ were selected to derive the zero-point. If the standard deviation of the zero points from these stars was greater than 0.3, the stars producing the most deviant zero points were replaced with other stars in the field. Errors were calculated from the variance in the sky aperture. The sky background was calculated using a clipped mean. The IRIS2 system most closely resembles the Mauna Kea Observatory (MKO) system. Equations (1) and (2) were used to transform between the MKO and 2MASS systems:

$$J_{\rm MKO} = -0.03 - 0.03(J - K_s) + J, \tag{1}$$

$$K_{\rm MKO} = -0.01 - 0.01(J - K_s) + K, \tag{2}$$

where J and K_s are given in the 2MASS system and $J_{\rm MKO}$ and $K_{\rm MKO}$ are given in the MKO system used by IRIS2.[1] Derived values of J- and K-band magnitudes are given in Table 3.

2.6 Stellar mass fitting

Stellar masses and SFRs were calculated using an spectral energy distribution (SED) fitting routine (Glazebrook et al. 2004) which employs the Baldry & Glazebrook initial mass function (IMF;
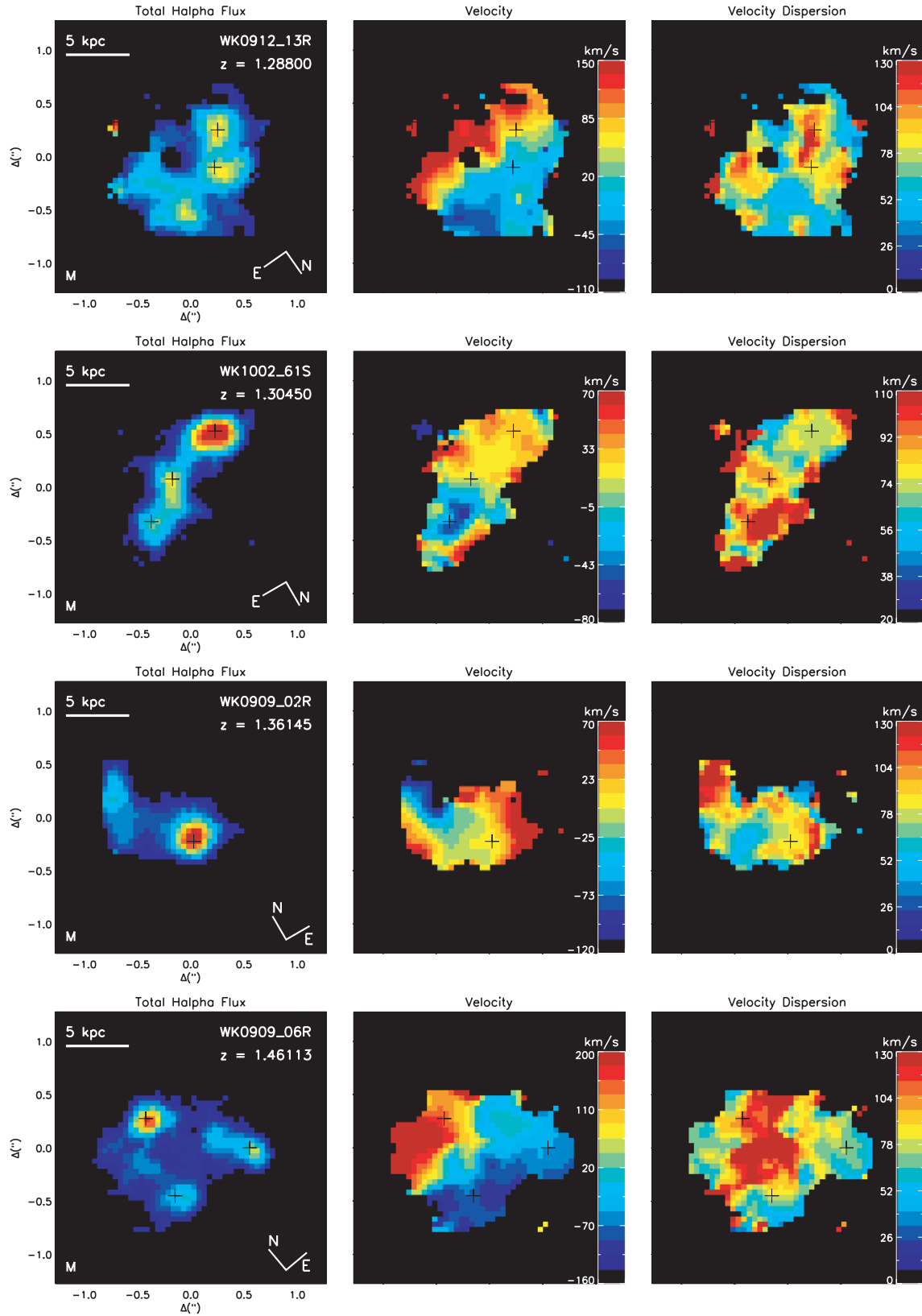
---

[1] http://www.aao.gov.au/iris2/

Figure 3. OSIRIS Hα kinematics. Left: Hα flux map; middle: velocity map from the systemic velocity; right: velocity dispersion map. The black crosses mark the peak(s) in Hα flux. Velocity shifts from the systemic redshift and velocity dispersion are measured in km s^{-1}. Compass at the bottom right of the left-hand panels shows the true orientation. Letters at the bottom left of the left-hand panels represent morphology classifications – M: multiple emission; E: extended emission; S: single emission. Objects are presented in the order based on the morphological classification described in Section 3.1.
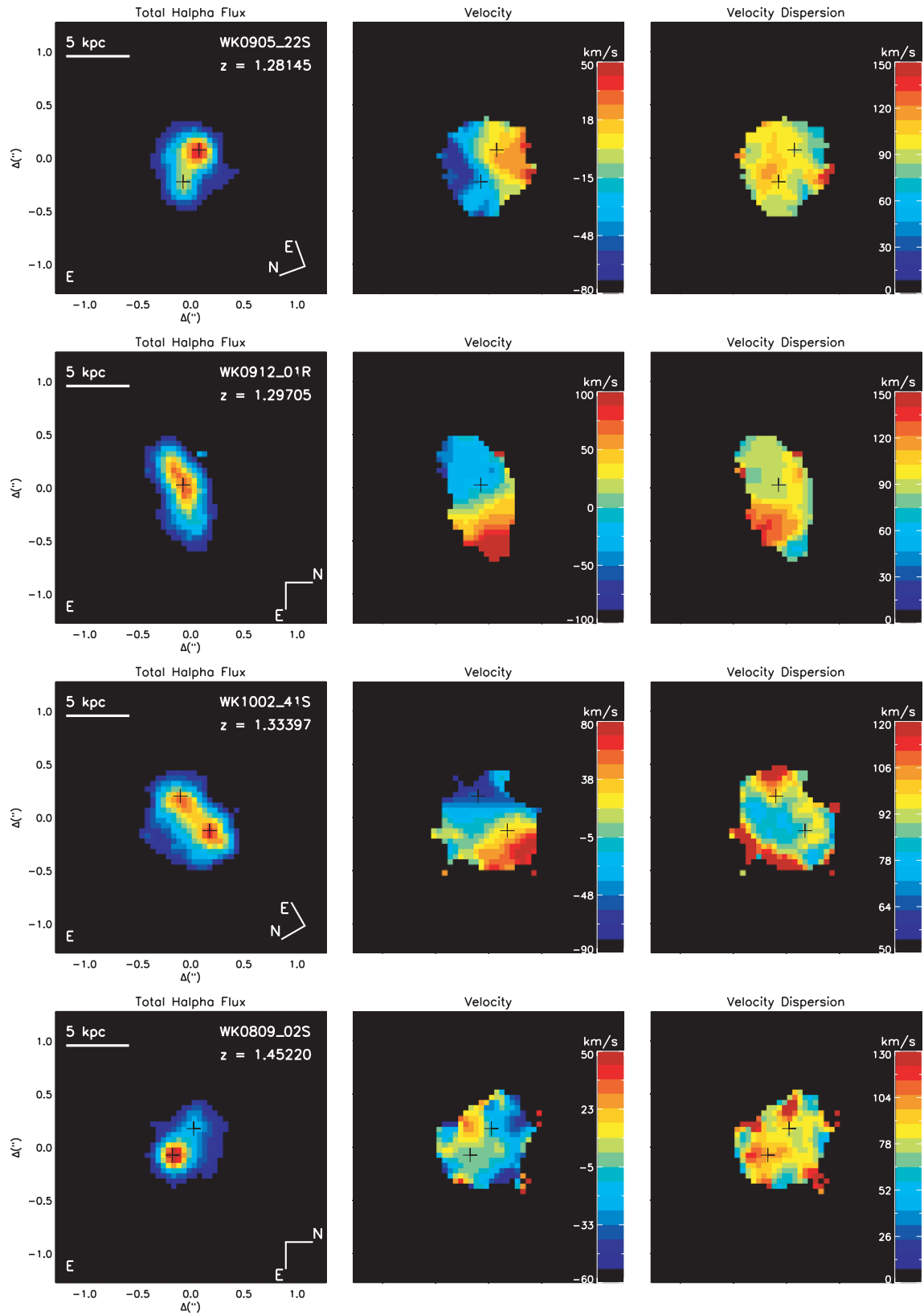
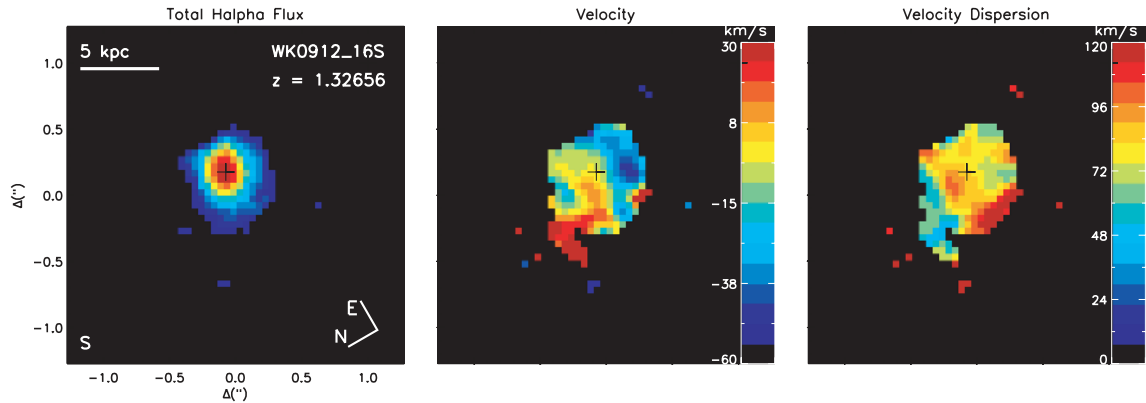**Figure 3** – *continued*
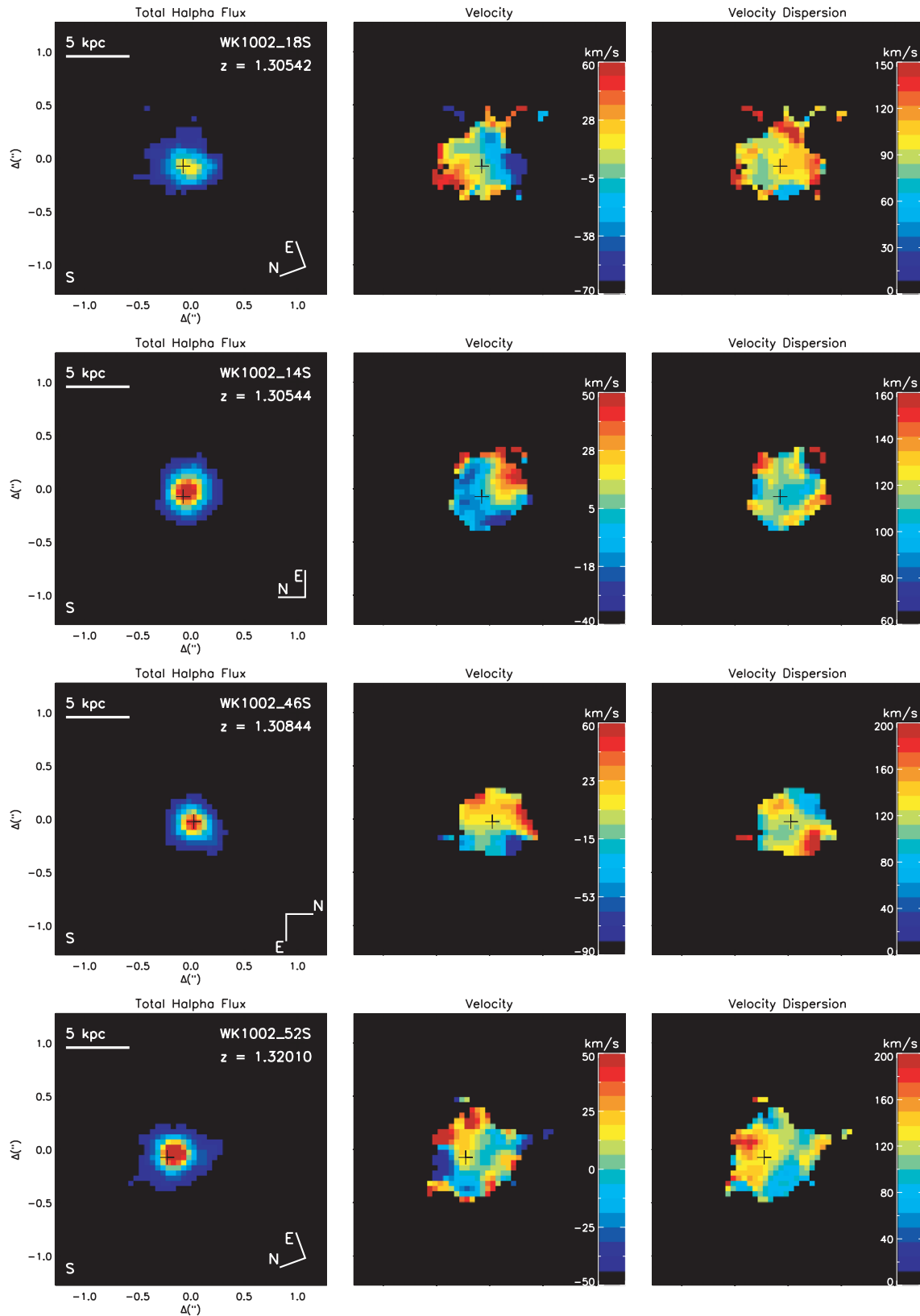
Figure 3 – *continued*

Figure 3 – *continued*

Table 3. IRIS2 observations of WiggleZ galaxies.

ID	Obs. date	J exp. time (s)	K exp. time (s)	J^a	K^a
WK0912_13R	2010/01	1350	4050	20.71	20.13
WK0909_06R	2010/01	2700	3360	20.77	19.98
WK0905_22S	2009/05	1350	1350	21.36	20.52
WK1002_41S	2010/01	1350	3600	21.30	20.57
WK0809_02S	2010/07	1950	. . .	20.66	. . .
WK1002_18S	2009/05	1350	2700	20.84	21.02
WK1002_14S	2009/05	1350	1350	20.69	20.20
WK1002_52S	2010/01	1350	3300	19.94	18.92
WK0912_16S	2010/01	1260	4050	21.79	21.93

^{a}Apparent AB magnitudes. The average error on J and K magnitudes is 0.11.

Baldry & Glazebrook 2003, hereafter BG03). The BG03 IMF fits local cosmic luminosity densities well, with a high-mass slope similar to the classical Salpeter IMF but with a more realistic break at $0.5\,M_{\odot}$. Hopkins & Beacom (2006) have shown that the BG03 IMF gives a better agreement between cosmic star formation histories and mass assembly.

Infrared JK data from IRIS2 were combined with multiband photometry available in WiggleZ fields, including *ugriz* from SDSS, *grz* from the RCS2 Survey and NUV from *GALEX*. Two-component modelling was adopted (using PEGASE.2 from Fioc & Rocca-Volmerange 1997 to calculate spectra) to assess the possible biases from starbursts on the calculated masses and to allow a range of dust extinction ($0 \leq A_V \leq 2\,\mathrm{mag}$) and metallicity ($0.0004 \leq Z \leq 0.02$). The primary component was modelled using SFR $\propto \exp(-t/\tau)$ with $\tau = 0.1, 0.2, 0.5, 1, 2, 4, 8$ and $500\,\mathrm{Gyr}$ (the first approximates an instantaneous starburst and the last a constant SFR). The full distribution function of allowed masses was calculated by Monte Carlo resampling of the photometric errors. The final masses and error bars, given in Table 5, represent the mean and standard deviation of this full distribution function. In the cases where observed UV, optical and NIR magnitudes were available the errors in the derived stellar masses are on average $\delta[\log(M_*[M_{\odot}])] = 0.15$. When NIR magnitudes were not available, the errors average $\delta[\log(M_*[M_{\odot}])] = 0.62$.

We do not use the models of Maraston et al. (2006) as Kriek et al. (2010) show a low contribution from TP-AGB stars for post-starburst galaxies at high redshift. For more information on the SED fitting see Glazebrook et al. (2004).

3 RESULTS

In Fig. 3 we present Hα spatial (left-hand panels) and kinematic maps of our 13 galaxies observed with OSIRIS with spatial extent ranging from 2 to 12 kpc. A broad range of morphologies and kinematics are observed with 8/13 galaxies showing some velocity shear and the remaining showing disturbed kinematic morphologies (middle panels). The dispersion maps for the entire sample are chaotic with peaks in velocity dispersion exceeding $100\,\mathrm{km\,s^{-1}}$ (right-hand panels). In the next subsections we will discuss the Hα morphology and kinematics, emission-line properties and masses of the sample. For convenience IDs are shortened and referred to by their last three unique digits.

3.1 Classification

We initially classified the galaxies into three groups based solely on Hα morphology: single emission, extended emission and multiple emission. Galaxies classified as single emission have a single resolved source of Hα emission: 16S, 14S, 18S, 46S and 52S. Systems classified as extended emission show multiple unresolved or extended components: 02S, 22S, 01R and 41S. Systems 02R, 06R, 13R and 61S are classified as multiple-emission galaxies, which have multiple, resolved regions of Hα emission. The centres of the separate components are marked in Fig. 3. These classifications are made for the purpose of discussing properties of galaxies with similar morphologies. The classifications are used to order tables and figures. Kinematic classifications are discussed in Section 4.

3.2 Kinematic quantities

A flux-weighted velocity dispersion (σ_{mean}) was calculated from the dispersion and flux across all spaxels. We define velocity dispersion by σ_{mean}, which is representative of the internal motions of the gas (Law et al. 2007; Green et al. 2010). For comparison, a line-of-sight velocity dispersion (σ_{net}) was calculated from the width of a Gaussian fit to the Hα emission of the integrated spectrum. The measured values of σ_{mean} are consistent with or slightly less than σ_{net}, as expected from velocity smearing. The values of σ_{mean} in this sample reach to $\sim 130\,\mathrm{km\,s^{-1}}$, and are typically higher than in the samples of Law et al. (2009) and Epinat et al. (2009). We note that the 0.15 arcsec smoothing described in Section 2.3 produces a $+10\,\mathrm{km\,s^{-1}}$ median boost compared to σ_{mean} calculated from the

Table 4. Hα kinematic and morphological properties.

ID	v_{shear}^a (km s^{-1})	σ_{mean}^b (km s^{-1})	σ_{net}^c (km s^{-1})	v_{shear}/σ_{mean}	$r_{1/2}^d$ (kpc)	Class^e
WK0912_13R	130.5 ± 11.0	81.6 ± 27.7	104.3 ± 27.1	1.6 ± 0.6	3.8	M
WK1002_61S	71.5 ± 10.7	85.1 ± 20.3	88.4 ± 4.4	0.9 ± 0.2	3.8	M
WK0909_02R	136.4 ± 6.1	87.9 ± 21.9	103.7 ± 15.5	1 ± 0.3	2.6	M
WK0909_06R	160.8 ± 2.4	92.6 ± 27.8	153.3 ± 8.4	1.6 ± 0.5	4.2	M
WK0905_22S	55.5 ± 6.5	98.2 ± 10.9	107.4 ± 3.3	0.6 ± 0.1	2.3	E
WK0912_01R	99.4 ± 7.1	98.6 ± 19.6	112.1 ± 11.0	1.3 ± 0.3	2.8	E
WK1002_41S	80.2 ± 5.4	91.4 ± 13.0	116.3 ± 5.9	1.7 ± 0.3	3.1	E
WK0809_02S	48.5 ± 9.4	92.7 ± 16.6	97.6 ± 13.8	0.4 ± 0.1	2.1	E
WK1002_18S	81.1 ± 17.5	102.1 ± 20.0	106.6 ± 6.8	0.7 ± 0.2	2.1	S
WK1002_14S	48.4 ± 9.5	113.7 ± 8.8	133.3 ± 4.8	0.5 ± 0.09	2.1	S
WK1003_46S	65.6 ± 16.7	124.8 ± 24.9	138.6 ± 9.6	0.5 ± 0.2	1.8	S
WK1003_52S	73.7 ± 18.2	125.4 ± 20.9	145.4 ± 8.1	0.7 ± 0.2	1.8	S
WK0912_16S	54.9 ± 12.9	85.1 ± 18.6	104.4 ± 9.1	0.7 ± 0.2	2.5	S

^{a}Velocity shear measured across the Hα velocity map as described in Section 3.2.
^{b}Flux-weighted mean velocity dispersion calculated from a Gaussian fit to the spectra of individual spaxels of the OSIRIS Hα detection.
^{c}Velocity dispersion calculated from a Gaussian fit to the integrated spectrum of the OSIRIS Hα detection.
^{d}Half-light radius of OSIRIS Hα emission in circular aperture.
^{e}Morphological classification – E: extended emission; M: multiple emission; S: single emission.

non-smoothed data which is less than the statistical error. We give the σ_{mean} values from the smoothed data in Table 4 for comparison to the literature.

We do not make a correction based on beam smearing resultant from the PSF, which can be a problem for interpreting kinematic observations at high redshift (e.g. Förster Schreiber et al. 2009; Law et al. 2009; Wright et al. 2009; Epinat et al. 2010). Although all observations were taken in LGSAO mode, with a PSF of FWHM ∼ 850 pc, Law et al. (2009) and Wright et al. (2009) note that beam smearing can still have the effect of reducing the maximum rotation velocity and inflating the velocity dispersion for edge on discs in particular. However, as the inclination is not well constrained in this study it is unclear when and what correction would be appropriate. The same authors note that beam smearing does not explain the high velocity dispersions of objects which show no rotational velocity structure.

The observed dispersion and luminosity of the WiggleZ sample continues the relationship, spanning over $0 < z < 3$, observed by Green et al. (2010) for star-forming galaxies, recreated in Fig. 4. The galaxies in the WiggleZ sample follow this relationship tightly with the highest dispersions and Hα luminosities of the IFS samples introduced in Fig. 1. Green et al. (2010) argue that the correlation seen implies SFR is the driving factor of the high velocity dispersion, not mass or gas fractions. Consequently, arguments that high velocity dispersions at high redshift are evidence for cold-flow accretion are weakened as the cold flows are no longer in place at the current epoch to produce the high dispersions observed in local galaxies.

A velocity shear was measured across each galaxy, $v_{shear} = 0.5(v_{max} - v_{min})$, following Law et al. (2009). In order to prevent biasing from outliers, v_{max} and v_{min} are calculated from the mean of the highest and lowest 5 per cent of the velocity map, respectively (Gonçalves et al. 2010). The values of v_{shear} underestimate the true rotational velocity of the gas in the cases that the galaxy extends to greater radii than detected by OSIRIS. The values of σ_{mean}, σ_{net}, v_{shear} and v_{shear}/σ_{mean} are given in Table 4. We do not find a correlation between velocity shear and stellar mass in this sample of 13 galaxies, in disagreement with the $z \sim 3$ sample of Law et al. (2009) and Lyman-break analogues at $z \sim 0.1$ (Gonçalves et al.
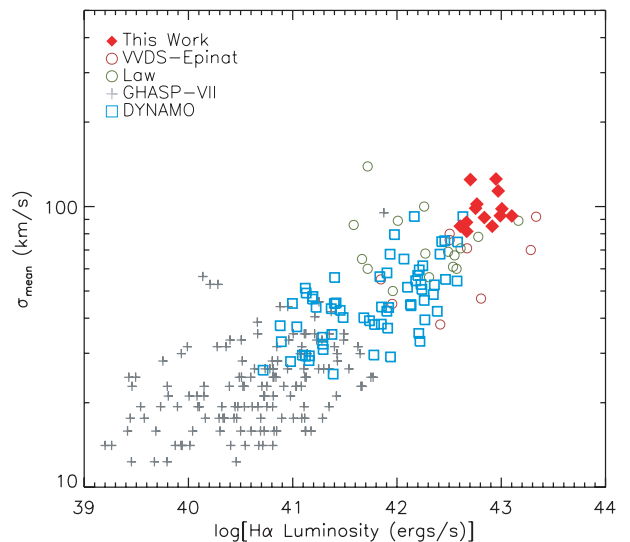

Figure 4. Flux weighted velocity dispersion as a function of $L_{H\alpha}$ from Green et al. (2010) with galaxies from this sample as red diamonds. The WiggleZ points extend this relationship to higher σ_{mean} and Hα luminosity.

2010). However, in the context of other star-forming galaxies at $1 < z < 3$ a positive correlation is seen, as shown in Fig. 5. The interpretation of the relationship is that stable rotation is more prevalent in galaxies that have assembled a relatively large stellar population. However, the addition of this sample does not affect the correlation originally published by Law et al. (2009). It is unclear if the velocity shear from all samples are comparable given the different spatial scales probed by OSIRIS and SINFONI and the different signal-to-noise ratio reached for each set of observations.

3.3 Star formation rate indicators

SFRs were measured from WiggleZ [O ii] and OSIRIS Hα luminosities. Because of uncertainties arising in the flux calibration of optical fibre spectroscopy, the WiggleZ [O ii] fluxes are only accurate to within 40 per cent due to systematic errors. OSIRIS Hα
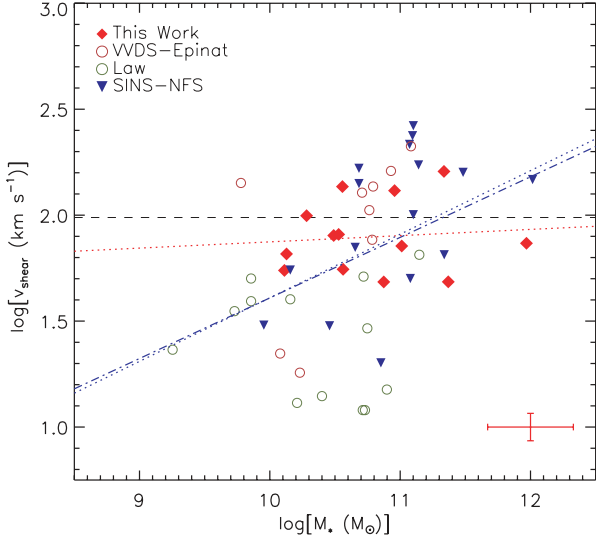
Figure 5. Logarithmic velocity shear as a function of logarithmic stellar mass for our 13 galaxies and galaxies from Law et al. (2009), Genzel et al. (2006, 2008), Förster Schreiber et al. (2006) and Epinat et al. (2009). Data are not corrected for inclination. All stellar masses are converted to the Salpeter IMF for ease of comparison with the literature. A median error for the WiggleZ points is plotted in red in the lower right-hand corner. The red dotted line is the best-fitting linear model to the 13 galaxies in our sample [$\log(v_{\mathrm{shear}}/\mathrm{km\,s^{-1}}) = 0.03\log(M_*/\mathrm{M_\odot}) + 1.58$], the blue dot–dash line is the best-fitting linear model to the data from all the samples [$\log(v_{\mathrm{shear}}/\mathrm{km\,s^{-1}}) = 0.25\log(M_*/\mathrm{M_\odot}) - 0.84$], the blue dotted line is the best-fitting linear model from Law et al. (2009) [$\log(v_{\mathrm{shear}}/\mathrm{km\,s^{-1}}) = 0.29\log(M_*/\mathrm{M_\odot}) - 1.25$] and the black dashed line is at the value of $\langle\log(\sigma_{\mathrm{mean}})\rangle$.

flux measurements are comparably more accurate and are thus used as the primary measure of the nebular star formation. SFR were calculated from Kennicutt (1998):

$$\mathrm{SFR_{O\,II}}\,[\mathrm{M_\odot\,yr^{-1}}] = \frac{1}{1.82}\frac{L_{\mathrm{O\,II}}\,[\mathrm{erg\,s^{-1}}]}{7.1\times10^{40}}, \qquad (3)$$

$$\mathrm{SFR_{H\alpha}}\,[\mathrm{M_\odot\,yr^{-1}}] = \frac{1}{1.82}\frac{L_{\mathrm{H\alpha}}\,[\mathrm{erg\,s^{-1}}]}{1.26\times10^{41}}, \qquad (4)$$

where the 1/1.82 converts to the BG03 IMF.

Further measurement of star formation is derived from the SEDs generated from the stellar mass fitting described in Section 2.5 (SFR$_{\mathrm{SED}}$). A dust extinction, $A_{\mathrm{V,SED}}$, is estimated from the SED fitting described in Section 2.6 and given in Table 5. The mean error on Av_{SED} is 0.2.

3.4 Metallicity

[N II] was detected in eight of the 13 galaxies in our sample. The detections and upper limits are used to investigate the metallicity and level of contamination from hosting an AGN by using the [N II]$\lambda6584$/Hα ratio. Metallicity was calculated from this ratio, as calibrated by Pettini & Pagel (2004),

$$12 + \log\left(\frac{\mathrm{O}}{\mathrm{H}}\right) = 8.90 + 0.57\times\log\left(\frac{[\mathrm{N\,II}]}{\mathrm{H}\alpha}\right), \qquad (5)$$

and given in Table 2. The metallicities of the sample are all subsolar and are consistent with the results of IFS samples at $z\sim1$–3 of Genzel et al. (2008), Stark et al. (2008), Law et al. (2009), Förster Schreiber et al. (2009) and Wright et al. (2009) and DEEP2 star-forming galaxies at $z\sim1.3$ (Shapley et al. 2005). The typical errors in $12 + \log(\mathrm{O/H})$ are 0.2.

Metallicity measurements calculated from equation (5) alone can be biased due to elevated levels of [N II] caused by AGN contamination. We look for this bias by constraining the position of the galaxies in this sample on the emission-line diagnostic, or Baldwin, Phillips and Terlevich (BPT) diagram (Baldwin et al. 1981), shown in Fig. 6. NIRSPEC observations of [O III]$\lambda\lambda5007$, 4959 and Hβ of four galaxies in the sample further quantify AGN contamination using the [O III]$\lambda5007$/Hβ ratio. Two of the [N II]/Hα measurements are upper limits (see column 5 of Table 2), and in all cases the [N II]/Hα ratios are significantly lower than the level expected for the given values of [O III]$\lambda5007$/Hβ if there was a significant component of AGN emission. The remainder of galaxies all lie to the left of $\log([\mathrm{N\,II}]/\mathrm{H}\alpha) = -0.6$, in the shaded grey region of Fig. 6. Although AGN contamination cannot be ruled out completely for these sources, their integrated nebular emission is clearly dominated by star formation.

3.5 Mass estimates

The sample stellar masses range from $9.8 < \log(M_*[\mathrm{M_\odot}]) < 11.7$, comparable to masses from other IFS samples covering the same

Table 5. Stellar properties.

ID	$\log[M_*(\mathrm{M_\odot})]$	A_V (mag)	SFR$_{\mathrm{H\alpha}}^a$ ($\mathrm{M_\odot\,yr^{-1}}$)	SFR$_{[\mathrm{O\,II}]}^b$ ($\mathrm{M_\odot\,yr^{-1}}$)	SFR$_{\mathrm{SED}}$ ($\mathrm{M_\odot\,yr^{-1}}$)	SSFR ($10^{-9}\,\mathrm{yr^{-1}}$)
WK0912_13R	10.7 ± 0.2	1.1 ± 0.3	20.3 ± 6.8	43.3 ± 0.9	116 ± 40.4	1.8
WK1002_61S	10.7 ± 0.7	0.2 ± 0.2	35.6 ± 2.3	69.0 ± 2.8	25.6 ± 13	2.9
WK0909_02R	10.3 ± 0.6	0.7 ± 0.4	20.2 ± 3.8	33.1 ± 0.8	57.4 ± 41.5	4.6
WK0909_06R	11.0 ± 0.2	0.8 ± 0.3	54.8 ± 3.9	120.3 ± 14.9	91.8 ± 48.7	2.09
WK0905_22S	10.3 ± 0.2	0.3 ± 0.2	44.0 ± 1.8	202.4 ± 23.8	44.6 ± 15.1	10
WK0912_01R	10.0 ± 0.6	0.5 ± 0.2	24.6 ± 3.2	59.0 ± 3.8	40.3 ± 13	11.2
WK1002_41S	10.2 ± 0.1	0.4 ± 0.1	29.9 ± 2.0	112.8 ± 5.7	60.3 ± 9.3	8.1
WK0809_02S	11.1 ± 0.6	0.0 ± 0.1	42.5 ± 7.7	29.7 ± 0.8	19.5 ± 6.9	1.5
WK1002_18S	10.2 ± 0.1	0.5 ± 0.1	25.3 ± 2.1	188.6 ± 14.2	64 ± 17.4	6.09
WK1002_14S	10.6 ± 0.2	0.3 ± 0.1	40.6 ± 1.9	43.9 ± 0.7	55.5 ± 16	4.5
WK1003_46S	9.8 ± 0.6	0.2 ± 0.3	22.0 ± 2.0	41.3 ± 4.8	22.4 ± 17.1	12.8
WK1003_52S	11.7 ± 0.1	0.0 ± 0.1	38.6 ± 2.7	103.7 ± 16.9	15.9 ± 2.2	0.3
WK0912_16S	9.8 ± 0.2	0.1 ± 0.1	17.6 ± 2.0	64.1 ± 6.8	12.6 ± 3.2	12

^{a}Star formation rates are estimated using a Baldry-Glazebrook IMF.

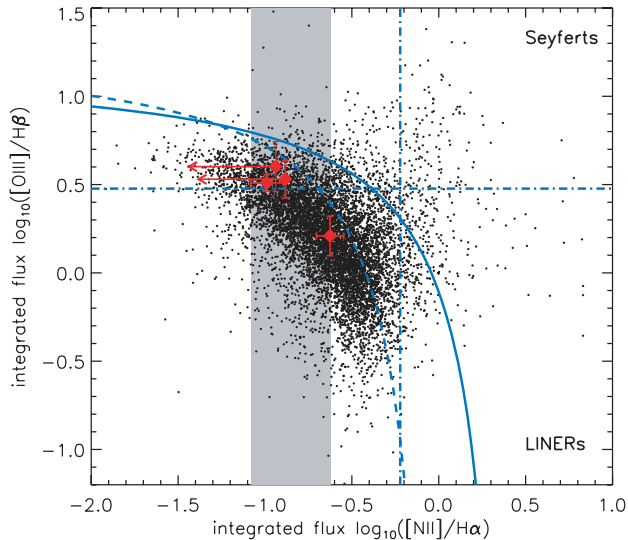^{b}Errors on the [O II] SFRs are statistical errors only.

Figure 6. The emission-line diagnostic diagram of Baldwin, Phillips & Terlevich (1981). The black points are WiggleZ galaxies and the red diamonds are 52S, 22S, 61S and 18S from this sample. The shaded grey area is the range containing the [N II]/Hα ratio for the remainder of the systems in this sample, the dashed curved line is the empirical line from Kauffmann et al. (2003), the solid curved line is the theoretical curve from Kewley et al. (2001) and the vertical and horizontal lines are used to identify Seyferts and low-ionization nuclear emission-line region galaxies (LINERs) as labelled. The WiggleZ subsample presented here is primarily in the region of the diagram where star formation is the dominant mechanism driving line emission.

redshift range ($1.2 < z < 1.7$; Epinat et al. 2009; Förster Schreiber et al. 2009; Wright et al. 2009) but with a higher $\langle M_* \rangle$ than high-redshift IFS samples ($z > 2$; Genzel et al. 2008; Law et al. 2009). No correlation is found between Hα morphology and mass; the three

most massive systems cover all three morphological classes, and the three lowest mass galaxies cover two morphological classes.

With stellar mass estimates we are able to identify where these systems lie relative to the main sequence of star formation (SFR versus M_*) as a function of redshift informing on the intensity of their star formation (e.g. Noeske et al. 2007; Rodighiero et al. 2010). If positioned above the main sequence, outside the limited range of SFRs at a given M_*, the star formation of the sample may be indicative of episodic variations rather than being associated with the larger population of continuous star-forming galaxies. Furthermore, the main sequence evolves with redshift in which higher SFRs were more typical in past epochs. Rodighiero et al. (2010) show that the mean specific SFR (SSFR $\equiv$ SFR/M_*) of galaxies decreases by a factor of $\sim$15 from $z = 2$ to $z = 0$ for the most massive galaxies. The main sequence for IFS samples is shown, as SFR versus M_*, in Fig. 7 in two redshift bins to account for this evolution. The SSFR is calculated, using SFR$_{H\alpha}$, and presented in Table 5.

In the lower redshift bin of Fig. 7, $1.2 < z < 1.7$, the star-forming galaxies from the SINS survey (Förster Schreiber et al. 2009) and Wright et al. (2009) form a sequence of star formation which scatter between the Great Observatories Origins Deep Survey (GOODS) $z = 1$ and $z = 2$ empirical relations. The WiggleZ points in contrast do not show an increase in SFR with mass and therefore the galaxies in this sample below $M_* = 5 \times 10^{10} \, M_\odot$ scatter above the main sequence and the galaxies with masses $> 5 \times 10^{10} \, M_\odot$ scatter below the main sequence. We note that the extinction correction applied here is derived from the SED fitting and future measurements of the dust content from far-infrared indicators will provide a more accurate correction affecting the location of this sample along the main sequence.

The high-redshift bin, $2.0 < z < 2.7$, shows a similar main sequence from the star-forming galaxies of the SINS survey and Law et al. (2009) which scatters around the GOODS $z = 2$ empirical relation. The mean SFR in the low-redshift bin ($\langle z \rangle \sim 1.52$) is a factor
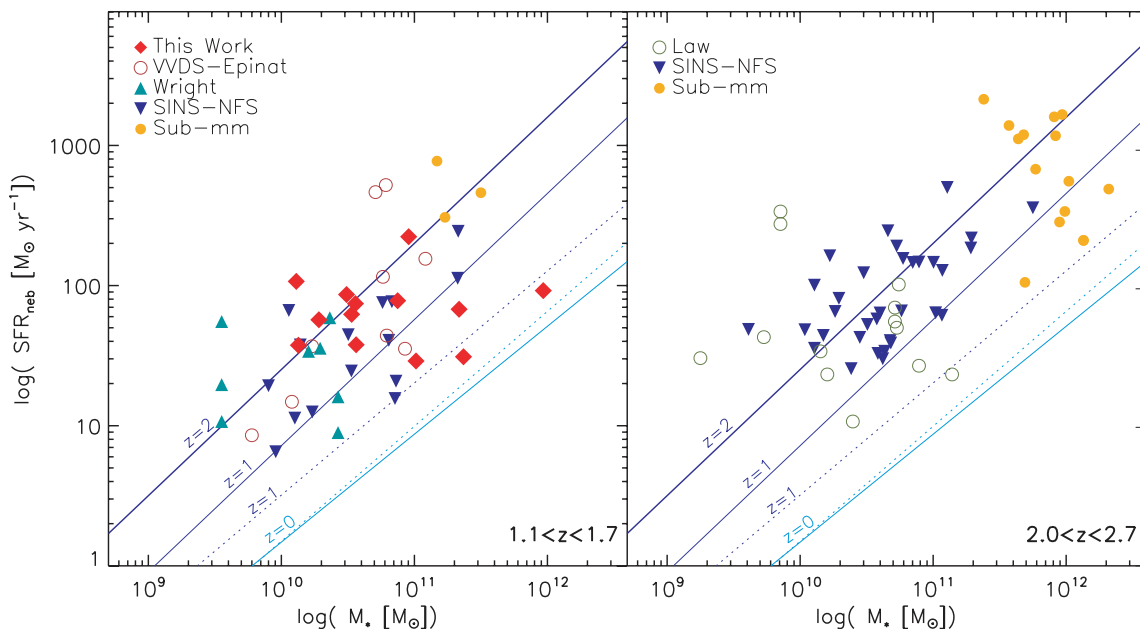

Figure 7. Hα SFRs of IFU samples at $z > 1$ as a function of stellar mass. Stellar masses and SFRs for all samples are converted to the Salpeter IMF for ease of comparison to the literature. The symbols are as described in Fig. 1. The solid lines are from the GOODS given in Elbaz et al. (2007) and Daddi et al. (2007). The dotted lines are from the Millennium Simulation (Springel et al. 2005; Croton et al. 2006) at redshifts $z = 0$ (light blue) and $z = 1$ (blue). An extinction correction is made from $E(B - V)_{SED}$.

of 0.7 less than the mean SFR in the high-redshift bin ($\langle z \rangle \sim 2.3$). SMGs are included in Fig. 7 for comparison to the IFS samples. SMGs are considered as the 'maximum starbursts' (Tacconi et al. 2008) with infrared determined SFRs $> 1000\,\mathrm{M_\odot\,yr^{-1}}$. For consistency, only SMGs with published nebular emission are included in the comparison to IFS results (Swinbank et al. 2004; Takata et al. 2006). SMG stellar masses are taken from Michałowski, Hjorth & Watson (2010). SFRs for all samples are calculated from measured nebular flux values with an extinction correction from $A_{\mathrm{V,SED}}$ and with a Salpeter IMF for consistency.

We find that the SMGs in the low-redshift bin are well matched statistically to the lower mass data presented here and higher on average than the other IFS samples. In the high-redshift bin the SMGs are offset in mass from the IFS samples. Unfortunately, the low number of SMGs with measured line emission limits an indepth comparison to this interesting galaxy population. However, initial comparisons to the available data indicate the WiggleZ sample presented here may be related to SMGs with more episodic star formation than LBGs at a given redshift and stellar mass.

3.6 Disc fitting

The velocity maps of the galaxies were modelled to determine whether the data are consistent with discs. Inclined disc models are generated varying the kinematic centre (x_0, y_0), the inclination (i, where $i = 0$ is a face-on disc), the position angle (ϕ), the systemic velocity (V_0), the plateau velocity (V_p) and the plateau radius (r_p) using the prescription of Begeman (1989):

$$V(x, y) = V_0 + V_c(r)\sin(i)\cos(\theta), \qquad (6)$$

where V_c is the circular velocity at a given radius from (x_0, y_0) and θ is the azimuthal angle in the plane of the galaxy, defined as

$$\cos(\theta) = \frac{-(x - x_0)\sin(\phi) + (y - y_0)\cos(\phi)}{r},$$
$$\sin(\theta) = \frac{-(x - x_0)\cos(\phi) + (y - y_0)\sin(\phi)}{r\cos(i)}. \qquad (7)$$

The circular velocity is defined as

$$V_c(r) = \begin{cases} V_p \frac{r}{r_p}, & r \le r_p, \\ V_p, & r > r_p \end{cases} \qquad (8)$$

for a flat rotation curve (Wright et al. 2007). The 'flat' disc model has been shown statistically to reproduce fitting parameters more successfully than the exponential disc, isothermal sphere and arctangent models in artificially redshifted IFS data (Epinat et al. 2010). The models are convolved with the observed PSF, modelled from a tip-tilt star observation and are fit to the data prior to the 0.15 arcsec smoothing to reduce the effects of beam smearing. The best-fitting

models were determined by minimizing the reduced chi-squared value (χ_R^2) using Monte Carlo Markov Chain methods. The parameter results of the best-fitting models, χ_R^2 values, and the average residual velocity are given in Table 6. Example models are shown in Fig. 8. The residual velocity, v_{res}, is calculated from the pixel average of the absolute value of the difference of the data and model.

The kinematic centre is not well constrained in single-emission galaxies, particularly in the single-emission galaxies that show no shear or have fewer spatial pixels. In these cases, specified in Table 4, the kinematic centre is fixed to the peak of Hα emission. Although the peak of Hα emission is not necessarily the dynamical centre of the galaxy, Wright et al. (2009) find that it is a reasonable approximation.

We find that 7/13 of our galaxies (06R, 01R, 13R, 41S, 22S, 14S, 18S) are well fit by a disc model. To determine which objects are well fit by this simple disc model we consider the velocity residual, reduced chi-square value and a qualitative measure of coherent velocity shear. We note that χ_R^2 is biased as the spaxels are correlated due to the intrinsic PSF and is not alone a reliable indicator. Furthermore, small fluctuations in the velocity map resulting from galactic winds and/or interactions between individual star-forming regions will inflate the residual and reduced chi-squared values as they are not accounted for in the model.

A known approximate degeneracy exists between V_p and i in the form $V_p\sin(i)$ in equation (6) (e.g. Begeman 1989; Epinat et al. 2009; Law et al. 2009). In previous low signal-to-noise ratio IFS work the inclination is set to a constant of $i = 45$ (Wright et al. 2009), however, Law et al. (2009) derive $i = 57.3$ as the correct average inclination between our line of sight to a given disc and the vector normal to the disc. The most robust method may be to fix the inclination to values derived from deep broad-band imaging (Epinat et al. 2009), however, we consider $V_p\sin(i)$ as one parameter in this study as we lack sufficiently deep imaging to determine it from photometry.

We find another degeneracy present in 41S, 14S and 13R between the plateau radius and plateau velocity. This degeneracy arises from the linear nature of the velocity gradients observed and is likely a consequence of not probing to faint enough surface-brightness emission to detect the kinematic turnover. A characteristic peak of velocity dispersion, a result of rapid unresolved change in velocity, would not be expected in the dispersion maps. Similarly, face-on and low-mass galaxies which have a low velocity gradient show a very faint or no central peak of velocity dispersion (Epinat et al. 2010). As a result we do not use the central peak of velocity dispersion as an indicator for disc classification.

As found in previous IFS studies of high-redshift galaxies the $v_{\mathrm{shear}}/\sigma_{\mathrm{mean}}$ (Table 4) values of this sample are approximately unity.

Table 6. Disc model parameter results.

ID	ϕ	$V_p\sin(i)$ (km s^{-1})	r_p (kpc)	V_0 (km s^{-1})	Residual (km s^{-1})	χ_R^2
WK0912_13R	25^{+331}_{-14}	73^{+64}_{-32}	2^{+20}_{-1}	8^{+14}_{-9}	3.2	1.97
WK0909_06R	53 ± 2	187 ± 7	1 ± 1	43^{+5}_{-6}	4.3	5.12
WK0905_22S	287^{+10}_{-6}	102^{+80}_{-26}	5^{+3}_{-7}	-7^{+32}_{-22}	3.5	2.27
WK0912_01R	226^{+21}_{-35}	83^{+49}_{-43}	18^{+6}_{-3}	-14^{+7}_{-8}	2.6	3.44
WK1002_41S	219 ± 14	141^{+126}_{-20}	10^{+6}_{-2}	-7^{+28}_{-26}	1.5	0.99
WK1002_14S[a]	320 ± 36	42^{+49}_{-30}	17^{+3}_{-17}	15^{+6}_{-5}	1.1	1.71
WK1002_18S[a]	140^{+58}_{-65}	24^{+32}_{-21}	16^{+8}_{-3}	28 ± 7	2.1	2.58

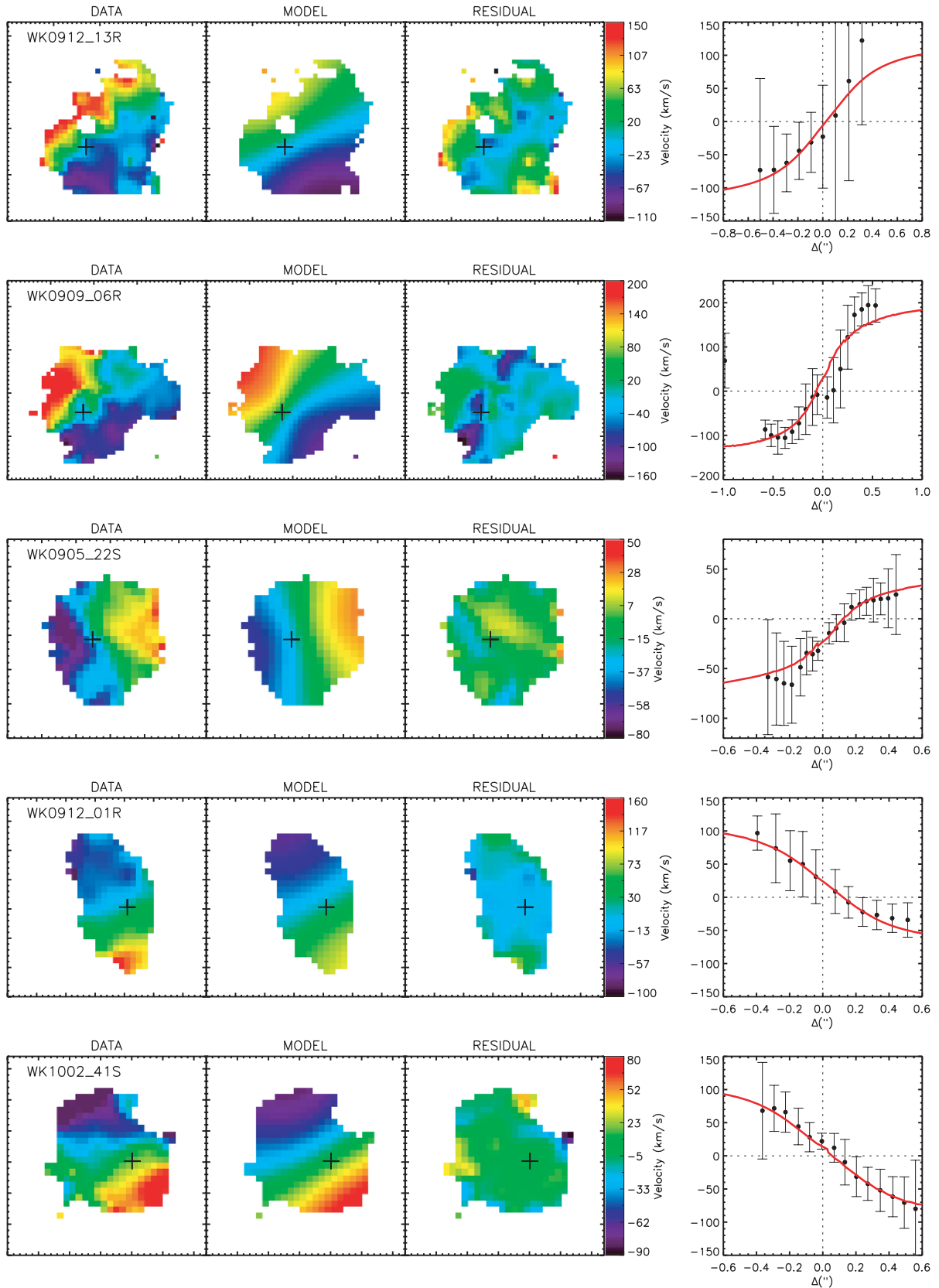[a]Kinematic centre fixed to peak of Hα flux distribution.

Figure 8. Disc fitting results for the 7/13 galaxies well fit by discs in the sample. The first panel shows the smoothed velocity map, the second panel shows the smoothed modelled velocity map fit to the unsmoothed data, the third panel shows the residual from the difference of panel 1 and panel 2 and the final panel shows the binned rotation curve across the major kinematic axis with the model overlaid in red.
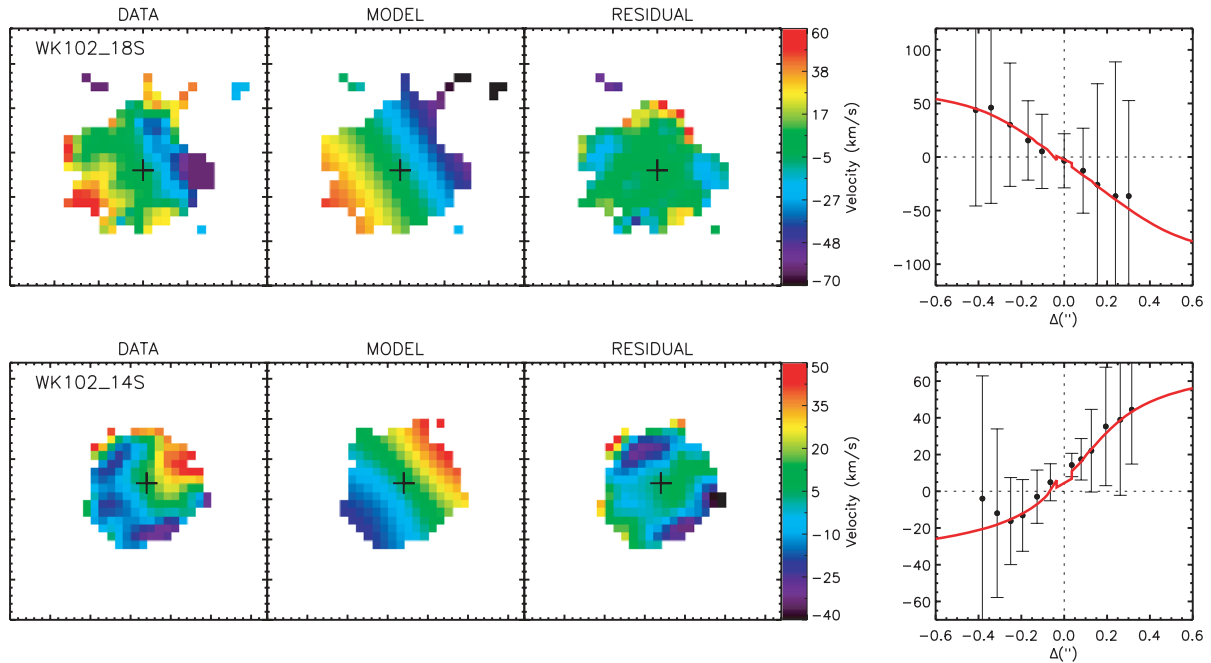
Figure 8 – *continued*

The v/σ measurement is often used to make a split between rotationally supported systems ($v/\sigma > 1$) and systems dominated by dispersion ($v/\sigma < 1$). In this sample 02R, 06R, 01R and 13R have $v/\sigma > 1$ while 02S, 22S, 16S, 46S and 52S have $v/\sigma < 1$ and 41S, 18S and 61S have $v/\sigma \approx 1$ within the errors. This correlates with the results of disc modelling in which 06R, 01R, 13R and 41S are well fit by discs and 02S, 16S, 46S and 52S are not well fit by discs. However, this picture fails for 22S and 14S which are well fit by discs but have $v/\sigma < 1$ and 02R which likely has an elevated v/σ as a result of an outflow rather than from the signature of rotational support (see Appendix A). It is likely that the discrepancy between these two methods is a result of the detection limit of the observations. The v_{shear} measurement probes only the inner star-forming regions of the galaxies and is not representative of the overall rotational velocity of the galaxy, thereby reducing the value of v/σ. Other factors are known to reduce the observed values of v/σ such as the foreshortening due to the inclination by a factor of $\sin i$ (Law et al. 2009). Because the inclination values in this study are poorly constrained this correction is not applied. As a result, more weight is given to the results of disc modelling rather than v/σ in classifying galaxies as being rotationally supported.

3.7 Surface brightness profiles

The effective radius was calculated by fitting convolved 1D Sérsic models to the Hα surface brightness profiles of single-emission galaxies. In order to fit model Sérsic profiles, the central spaxel of the galaxy or star-forming complex was first identified from the peak of the flux maps. The distance to the remaining spaxels was calculated from the central point assuming a circular profile, reducing the number of free parameters by setting the aspect ratio to unity and position angle to zero. Individual measurements are averaged in radial bins. The models were convolved with the PSF. The best-fitting Sérsic profile model was determined by minimizing the chi-squared value (χ^2) with three free parameters, n, r_0 and Σ_0, where n is the Sérsic index, r_0 is the effective radius and Σ_0

Table 7. Surface brightness fitting.

ID	n	r_{eff} (kpc)
	Hα images	
WK0909_02R	$1.0^{+0.1}_{-1.6}$	$0.6^{+0.2}_{-1.6}$
WK1002_18S	0.8 ± 0.1	1.9 ± 0.4
WK1002_14S	$0.9^{+0.03}_{-0.1}$	$0.9^{+0.1}_{-0.2}$
WK1003_46S	1.0 ± 0.1	$0.7^{+0.1}_{-0.2}$
WK1003_52S	$2.0^{+0.6}_{-0.1}$	0.4 ± 0.1
WK0912_16S	$0.5^{+0.1}_{-0.3}$	$1.5^{+0.2}_{-0.6}$
	RCS2 rest-frame UV images	
WK0912_13R	$0.6^{+0.1}_{-1.8}$	$4.6^{+2.9}_{-2.5}$
WK0909_02R	$1.0^{+0.2}_{-0.6}$	6.1 ± 2.0
WK0909_06R	0.4 ± 0.3	$3.4^{+2.6}_{-1.1}$

is the surface brightness at the effective radius. We assume this simple model as the inclination and position angle determined in Section 3.6 are not well constrained.

The fitted results are shown in Table 7 with r_{eff} ranging from $0.4 < r_{eff} < 1.9$ kpc and n ranging from $0.5 < n < 2.0$. An example model fit to the data is shown in Fig. 9. It is not completely understood what the flux profile of Hα emission reveals about the parent galaxy as Sérsic profiles are more commonly fit to broad-band emission representative of continuum emission from continuous star formation (Sérsic 1968). However, the SINS survey obtained deep rest-frame optical images of six irregular galaxies in their sample and found surprisingly good morphological agreement between Hα and broad-band images (Förster Schreiber et al. 2011). They find the Sérsic parameters of Hα emission and H-band emission (rest-frame optical) are consistent for the six galaxies with a difference on average of 0.08 for the Sérsic index and agreement within 3 per cent for r_{eff}. The Sérsic indices are comparable to our Hα results with $n < 1$ in all cases, however, they find greater effective radii with
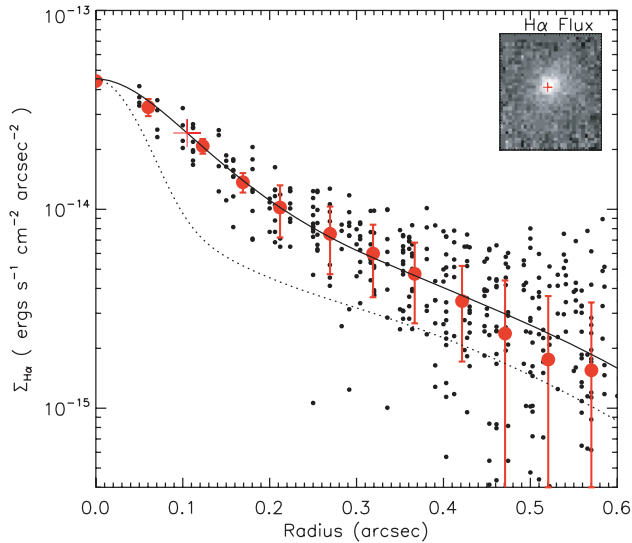
Figure 9. Example of surface brightness modelling results for 14S. The black points represent the flux in each spaxel from the peak of emission marked with the red plus sign in the Hα image of the galaxy in the top right-hand corner. The red circles represent binned points, the black solid line is the best-fitting Sérsic model and the black dotted line is a fit to the flux profile of a tip-tilt star observed with OSIRIS.

$r_{eff} > 2$ kpc in all cases, most likely due to the coarser resolution from their non-AO-corrected observations.

The fitting method described above is applied to available r-band images from RCS2 only, as galaxies are unresolved in SDSS images. The RCS2 images, taken in average seeing of 0.7 arcsec, are sufficient to fit Sérsic profiles to three of 13 systems of the sample. We obtain results in the range $0.2 < n < 1.0$. A direct comparison to the Hα Sérsic parameters, however, is not possible as the only RCS2 data available is of extended or multiple-emission galaxies. Deeper imaging of the whole sample is needed to reveal whether the underlying stellar population probed by the rest-frame optical for these galaxies follows the morphology of the Hα emission.

3.7.1 Radii

We note that radius is a particularly difficult property to measure robustly and consistently with a variety of methods used in the literature. We calculate the kinematic plateau radius, r_p, from disc modelling and the effective radius, r_{eff}, from surface brightness profile fitting. The r_{eff} values presented are consistent with the sample of Law et al. (2009), $0.6 \leq r \leq 1.6$ kpc, but are smaller than most other samples (e.g. Wright et al. 2009: $2.1 \leq r \leq 3.9$ kpc; Förster Schreiber et al. 2009: $1.2 \leq r \leq 7.5$ kpc; Epinat et al. 2009: $1.2 \leq r \leq 5.5$ kpc). The half-light radius, $r_{1/2}$, is also estimated directly from the data by determining the size of the circular aperture needed to enclose half the Hα light from the centre of emission, and is given in Table 4. In some cases $r_{1/2}$ is the best measure of radius as neither r_{eff} or r_p are able to be measured due to irregular morphologies and kinematics. The $r_{1/2}$ values are greater on average than the r_{eff}, likely due to noise, and are comparable to the samples of Wright et al. (2009) and Epinat et al. (2009).

4 DISCUSSION

The sample presented here was selected from the WiggleZ survey for strong UV and nebular luminosities. The luminosity, mass, SSFR and v_{shear} are more comparable to the $z > 2$ subset of the

SINS survey than the samples at the same redshift, but more comparable in size to the $z \sim 2$ sample from Law et al. (2009). Like other IFS surveys we find a range of kinematics and morphologies with high velocity dispersions on average ($\langle \sigma_{mean} \rangle = 98$ km s^{-1}), yet the uniqueness of this sample is derived from the range of Hα morphologies with resolved kpc-size star-forming regions and ultracompact Hα emission of the single-emission galaxies.

However, IFS samples are all selected differently and may not be directly comparable. The SINS survey observes galaxies found from a variety of selection techniques including optical colour selected 'BX/BM' galaxies (Steidel et al. 2004), infrared colour selected 'BzK' galaxies (Daddi et al. 2004), Lyman break selected galaxies (LBGs) and bright submillimetre galaxies (SMGs). Epinat et al. (2009) select their galaxies from the magnitude complete VIMOS-VLT Deep Survey (VVDS), while Wright et al. (2009) observe BM galaxies, and Law et al. (2009) observed BX galaxies. While the WiggleZ sample was not selected by any of these methods, the SEDs of the sample imply that they could be classified as BM galaxies, BzKs and LBGs. Because IFS surveys are observationally expensive we are working with low number statistics and we must use the samples available for comparison as we cannot follow up mass or luminosity complete samples at high redshift.

The initial classification of this sample was based on Hα morphology into three groups: single emission, extended emission and multiple emission. A reclassification is now considered based upon the properties discussed in Section 3 in the context of disc formation at high redshift and a merger sequence. However, it is a challenge to distinguish between a galaxy merger and the merger of massive subclumps embedded within a rotating disc and similarly to distinguish between a merger remnant and a pseudo-bulge formed from the collapse of massive subclumps. Below we explore models of both disc formation and merger events at high redshift. We use the kinematic properties, masses, sizes, etc. to differentiate between the dominant formation mechanisms for the WiggleZ galaxies sample presented here.

4.1 The merger hypothesis

With separations of 3–10 kpc the Hα complexes may be sites of multiple regions of star formation merging from different parent galaxies. Kinematic quantities need to be utilized to find support for this hypothesis as deep imaging of diffuse continuum emission is unavailable to reveal tidal features characteristic of mergers. We analyse here a scenario in which our sample form a merger sequence with pre-, ongoing and post-mergers.

In this scenario the multiple-emission galaxies are the initial stages of mergers when star formation in separate galaxies can still be spatially differentiated. The extended-emission galaxies are the next stage in the sequence representing ongoing merging activity (or pre-mergers with component confusion due to projection effects). The final stage in the proposed merger sequence is the single-emission galaxies representing merger remnants with high dispersions and SFRs.

Velocity dispersion maps provide some evidence indicating that we are seeing separate kinematic components merging. The observed peaks in dispersion may correspond to centres of individual galaxies or be a result of shock fronts between merging systems. Systems 41S and 61S show multiple peaks in velocity dispersion correlated with the brightest regions of emission, indicative that the system is an early-stage merger where each galaxy has a peak in velocity dispersion corresponding to an unresolved component. However, the peaks in dispersion could also arise from winds from

the brightest regions (Genzel et al. 2011). Systems 13R and 06R show multiple peaks in velocity dispersion correlated with the gas between the brightest regions of emission, indicative of the turbulence occurring from the interaction of the gas from the merging galaxies in this scenario or the effect of fitting substructure along the line of sight with a single Gaussian.

The majority of IFS results classified as mergers show velocity maps where the velocity does not vary smoothly across the source but rather show a quick turnover within a resolution element or less (Nesvadba et al. 2008; Law et al. 2009; Wright et al. 2009). An ideal example, presented in Nesvadba et al. (2008), is a merging system observed as two unresolved 'clumps' of [O III] emission with a step in the velocity map between both components. This step function, observable with AO resolution, is not present in the kinematics presented here.

The single-emission galaxies in this scenario could be merger remnants. This comparison is particularly difficult as merger remnants produced in simulations show a wide range of kinematic and morphological properties with observables sensitive to the initial mass ratio of the merger (Naab & Burkert 2003). However, the majority of remnants are slow rotators (with $v/\sigma < 1$), and have high velocity dispersions and minor axis rotation (Naab & Burkert 2003; Cox et al. 2006; Bois et al. 2010). These properties could be used to describe 22S, 16S, 14S, 18S and 46S (although major and minor axes cannot be distinguished). These galaxies show some indication of rotation but with very low amplitudes ($v_{\rm shear} \sim 40\,{\rm km\,s^{-1}}$). However, it is difficult to distinguish merger remnants and discs. Some simulations even find that a low percentage of remnants also have disc-like isophotes (Naab & Burkert 2003).

Finally, a fraction of the sample, particularly the lower mass galaxies, is found above the 'main sequence' of star formation (Fig. 7), which indicates they may be undergoing a burst of star formation typical of a gas poor or minor merger event (Noeske et al. 2007).

Unfortunately, surface brightness detection limits of OSIRIS may introduce a selection effect of detecting only the brightest objects in merging systems. This effect can be seen in Fig. A1(b) of Appendix A for object 02R where an outflow or companion is seen in the RCS2 image but not detected in the Hα OSIRIS image. Classification errors may arise as a result of this effect. Deep broad-band imaging of all sources will help to reveal merging companions.

4.2 The clumpy disc hypothesis

We investigate the scenario where the data presented here represent different stages of the clumpy disc models of the EBE08 simulations. In this context galaxies with multiple regions of emission represent the early phases of disc formation when gravitational instabilities result in multiple star-forming complexes embedded within a disc galaxy. As turbulent speeds decrease relative to the rotational speed of the disc, the clumps migrate towards the centre on a timescale of ~1 Gyr, represented here by the galaxies with extended emission. Finally, the clumps coalesce and form a slowly rotating pseudo-bulge (Noguchi 1999; Bournaud, Elmegreen & Elmegreen 2007; EBE08; Dekel, Sari & Ceverino 2009b; Krumholz & Dekel 2010), represented here by galaxies with a single spherical emission profile.

The morphologies of multiple emission systems, 06R, 13R and 61S (Fig. 3) are well matched to the early stages of clumpy disc formation ($t = 175$–$450\,{\rm Myr}$). Systems 06R and 13R are well fit by disc models. The clump velocities follow the global velocity structure of the galaxy as seen in Fig. 8, where the major axis of

rotation cuts across multiple clumps revealing no corresponding deviation in the rotation curves (Immeli et al. 2004b).

The morphologies of 02S, 22S, 41S and 01R are either consistent with the system being observed at the clump coalescence phase ($t = 600$–$800\,{\rm Myr}$) or the result of projection effects. Systems 02S and 22S, each show two close components which can be distinguished when fitting surface brightness profiles, while 41S and 01R have single bright extended regions where multiple components cannot be differentiated visually or from surface brightness profiles. 22S, 41S and 01R are well fit by disc models whereas 02S has a flat velocity map with a peak in dispersion corresponding to the brightest peak in Hα emission. The fainter peak of emission may be a signature of a galactic outflow resulting in confusion in classification.

Star-forming regions within a disc should have similar or consistent metallicities as they are evolving within the same conditions as predicted by theoretical models for discs at high redshift (Immeli et al. 2004a). In a major or minor merger no similar correlation is expected in the metallicities of each galaxy. By integrating the light of each clump, the clump metallicities are calculated from equation (5). Metallicities of clumps in 06R and 61S are equal within the errors, as predicted for the early stages of disc fragmentation. At clump coalescence metallicities of individual clumps would be consistent as seen in 02S and 22S. Although this supports current theories, $12 + \log{\rm (O/H)}$ varies little across the sample ($\Delta[12 + \log{\rm (O/H)}] \sim 0.26$).

Compact single-emission galaxies 14S, 16S, 18S, 46S and 52S have morphologies well matched to the later stage of simulated formation when the clumps have collapsed to form a bulge ($t = 1000\,{\rm Myr}$). The dispersions of 14S, 46S and 52S are the highest in the sample and are consistent with EBE08 bulges, predicted to form by clump coalescence and become slow rotators with high turbulence of $\sigma_{\rm los} \sim 130\,{\rm km\,s^{-1}}$ in their inner regions. Systems 14S, 16S and 18S all show velocity gradients with amplitudes less than $70\,{\rm km\,s^{-1}}$. The bulge density profiles in the EBE08 models are well fit by Sérsic profiles of $n \sim 4$ in the inner 500 pc and $n > 2$ at greater radii. While we do not resolve the inner 500 pc we do resolve to 650–750 pc and find $n < 2$ in all cases for the Hα emission.

Velocity dispersion maps in this sample do not show characteristic central peaks in velocity dispersion observed in IFS studies in both local (de Zeeuw et al. 2002) and high-redshift (Genzel et al. 2006; Förster Schreiber et al. 2009) disc galaxies and therefore cannot be used as an indicator for disc classification. As discussed in Section 3.6, this peak in velocity dispersion can be attributed to beam smearing across the inner regions of the velocity turnover of the galaxy. However, because we are observing only the central region of rotation and have a small PSF as a result of using LGSAO, a dispersion peak is not expected.

Furthermore, if we model the velocity dispersion using the equation for a thick or compact disc (Binney & Tremaine 2008):

$$\sigma \sim \frac{h_{\rm z} V_{\rm c}(r)}{r}, \tag{9}$$

where $h_{\rm z}$ is the disc scaleheight, the expected model would give a constant, featureless dispersion map within the plateau radius ($r \leq r_{\rm p}$). This would be consistent with galaxies 41S, 14S and 13R where a plateau velocity is never reached. In this case the observed variations in velocity dispersion are more likely a result of random perturbations within the centre of the disc or local perturbations due to clumps.

The simulations of EBE08 and others that model and evolve these galaxies have mainly been developed with sticky-particle codes (Noguchi 1999; EBE08) which only model the cold gas associated

with the cold cloud medium. Immeli et al. (2004a,b) do include a hot phase to their simulation allowing the galaxy models to track stellar ages and metallicities providing observables that can be tested. Furthermore, the initial conditions of such models require the discs to have very high velocity dispersions to mimic observational results at these redshifts, making it difficult to distinguish inputs and outputs of the models. More realistic models are needed for a more rigorous comparison. Regardless of these limitations the data are well matched to the available models.

5 CONCLUSION

We favour the clumpy disc model over the merger sequence model. We find 7/13 of the sample is well modelled by a disc and we find that clumps found in galaxies with multiple regions of emission do not strongly affect the kinematic fields. This provides observational evidence for the models of EBE08 which provide an explanation for the irregular morphologies seen at high redshift.

However, whilst natural to attempt to identify kinematic observations as discs or mergers, as been attempted here, this simplified picture of galaxies becomes increasingly fallible at high redshift. More than half of the galaxy kinematics in this sample are well-described by disc models, however, it is important to be cautious of definitive kinematic classifications. For example, Epinat et al. (2010) provide evidence that up to 30 per cent of disc galaxies may be misclassified as perturbed rotators or complex kinematics with current classification schemes.

It is likely that we are seeing a variety of mechanisms at work which cannot be broken down into simply discs and mergers. Even if disc instability is a dominant mechanism in star formation histories at high redshift, as we find here, the discs are still likely to undergo mergers in their lifetime further complicating kinematic interpretations. Lemoine-Busserolle et al. (2010), for example, observe a galaxy pair with separation of 12 kpc with one galaxy in the pair classified as a disc with velocity gradient of $\sim$91 km s^{-1} and the other galaxy classified is compact and likely dominated by AGN. It is unclear how to classify this system, which has multiple kinematic components. Furthermore, with such small number statistics, the varying kinematics across multiple IFS samples could be due to varying properties amongst the galaxies selected and instruments used, making it difficult to compare results.

The global properties of the sample, the most luminous population, studied at $z \sim 1.3$ with IFS, are in surprising agreement with a model of unstable discs. We agree with Law et al. (2009) that statistically all high-redshift galaxies cannot be mergers. Models show that on average the enhancement of SFR in a merger is only a factor of a few and lasts 200–400 Myr with peak enhancement lasting for less than 100 Myr (Di Matteo et al. 2008; Teyssier, Chapon & Bournaud 2010). It has been shown locally that all ultraluminous infrared galaxies (ULIRGs) are mergers (Duc, Mirabel & Maza 1997) and it is therefore possible a high-redshift subset of galaxies are also exclusively mergers. However, galaxies on average formed their stars more rapidly in the past implying the need for an evolving definition of what makes more luminous galaxies 'extreme'. We therefore stress the importance of the bolometric luminosity in knowing if the sample presented here fall on or above the main sequence of star formation at this redshift to aid in making generalizations about galaxy populations at $z > 1$.

Discerning the dust content will aid in a better understanding of their star formation histories. Such moderate to high mass, gas rich, intensely luminous galaxies are reminiscent of local ULIRGs and $z \sim 2$–3 SMGs. However, critical to making this link is to determine their far-infrared and submm SEDs, and enabling the measurement of their bolometric luminosities and dust content. Such quantities will inform on whether these galaxies are dust-enshrouded starbursts or 'dust-free' late time protogalaxies. We will present Herschel data in a future paper that will address the dust content in this sample.

We expect to see signatures of outflows in these systems as galactic scale winds are expected in galaxies forming stars at >5 M$_\odot$ yr^{-1} and are seen in 75 per cent of ULIRGs (Veilleux, Cecil & Bland-Hawthorn 2005). Previous studies have detected galactic winds with IFS (high z: Shapiro et al. 2009; Swinbank et al. 2009; Alexander et al. 2010; local: Sharp & Bland-Hawthorn 2010). The high dispersions to the edges of 02S, 52S and 02R are real and not an inflation from lower signal-to-noise ratio data. This increase in dispersion towards the edges most likely indicates the presence of galactic winds which add an underlying broad component of Hα (Veilleux et al. 2005). The influence of winds on this sample will be further discussed in a subsequent paper.

Measuring the properties of the individual clumps including size, metallicity, SFR and velocity dispersion to compare to local samples will be important to testing models of clumpy disc formation. Only on order $\sim$10 clumps have been resolved with IFS studies using lensing and a further $\sim$10 resolved or marginally resolved within the SINS survey (Genzel et al. 2011). The properties of the 10 clumps identified in these systems will be presented in our next paper.

In this paper we

(i) present kinematic data of 13 star-forming galaxies at $z \sim 1.3$, selected from the WiggleZ Dark Energy Survey, of better or comparable resolution than previous studies;

(ii) extend the trend of Green et al. (2010) to higher SFRs and higher dispersions between $1 < z < 2$ (Fig. 4);

(iii) find the most luminous star-forming galaxies at this redshift show a variety of star-forming morphologies with a high incidence of star formation in discs;

(iv) identify clumps of 1–2 kpc in size at $z \sim 1.5$ that are resolved kinematically with LGSAO IFS without aid of lensing;

(v) conclude the clumps in multiple-emission galaxies follow the overall kinematics of the system, and find a high incidence of velocity gradients consistent with rotation lending support of the clumpy disc scenario of EBE08 over the major merger scenario.

cooperation with the Centre National d'Etudes Spatiales of France and the Korean Ministry of Science and Technology.

REFERENCES

Abraham R. G., Tanvir N. R., Santiago B. X., Ellis R. S., Glazebrook K., van den Bergh S., 1996, MNRAS, 279, L47

Adelman-McCarthy J. K. et al., 2006, ApJS, 162, 38

Alexander D. M., Swinbank A. M., Smail I., McDermid R., Nesvadba N. P. H., 2010, MNRAS, 402, 2211

Baldry I. K., Glazebrook K., 2003, ApJ, 593, 258 (BG03)

Baldwin J. A., Phillips M. M., Terlevich R., 1981, PASP, 93, 5

Begeman K. G., 1989, A&A, 223, 47

Binney J., Tremaine S., 2008, in Binney J., Tremaine S., eds, Galactic Dynamics, 2nd edn. Princeton Univ. Press, Princeton, NJ, Chapter 2

Blake C. et al., 2011, MNRAS, 415, 2892

Bois M. et al., 2010, MNRAS, 406, 2405

Bournaud F., Elmegreen B. G., Elmegreen D. M., 2007, ApJ, 670, 237

Cavanagh B., Hirst P., Jenness T., Economou F., Currie M. J., Todd S., Ryder S. D., 2003, in Payne H. E., Jedrzejewski R. I., Hook R. N., eds, ASP Conf. Ser. Vol. 295, Astronomical Data Analysis Software and Systems XII. Astron. Soc. Pac., San Francisco, p. 237

Conselice C. J., Bershady M. A., Dickinson M., Papovich C., 2003, AJ, 126, 1183

Cox T. J., Dutta S. N., Di Matteo T., Hernquist L., Hopkins P. F., Robertson B., Springel V., 2006, ApJ, 650, 791

Croton D. J. et al., 2006, MNRAS, 365, 11

Daddi E., Cimatti A., Renzini A., Fontana A., Mignoli M., Pozzetti L., Tozzi P., Zamorani G., 2004, ApJ, 617, 746

Daddi E. et al., 2007, ApJ, 670, 156

Davies R. I., 2007, MNRAS, 375, 1099

Dekel A. et al., 2009a, Nat, 457, 451

Dekel A., Sari R., Ceverino D., 2009b, ApJ, 703, 785

de Zeeuw P. T. et al., 2002, MNRAS, 329, 513

Di Matteo P., Bournaud F., Martig M., Combes F., Melchior A., Semelin B., 2008, A&A, 492, 31

Drinkwater M. J. et al., 2010, MNRAS, 401, 1429

Duc P., Mirabel I. F., Maza J., 1997, A&AS, 124, 533

Eggen O. J., Lynden Bell D., Sandage A. R., 1962, ApJ, 136, 748

Elbaz D. et al., 2007, A&A, 468, 33

Elmegreen B. G., Elmegreen D. M., 2005, ApJ, 627, 632

Elmegreen B. G., Bournaud F., Elmegreen D. M., 2008, ApJ, 688, 67 (EBE08)

Engel H. et al., 2010, ApJ, 724, 233

Epinat B. et al., 2009, A&A, 504, 789

Epinat B., Amram P., Balkowski C., Marcelin M., 2010, MNRAS, 401, 2113

Erb D. K., Steidel C. C., Shapley A. E., Pettini M., Adelberger K. L., 2004, ApJ, 612, 122

Erb D. K., Steidel C. C., Shapley A. E., Pettini M., Reddy N. A., Adelberger K. L., 2006, ApJ, 646, 107

Fioc M., Rocca-Volmerange B., 1997, A&A, 326, 950

Förster Schreiber N. M. et al., 2006, ApJ, 645, 1062

Förster Schreiber N. M. et al., 2009, ApJ, 706, 1364

Förster Schreiber N. M., Shapley A. E., Erb D. K., Genzel R., Steidel C. C., Bouché N., Cresci G., Davies R., 2011, ApJ, 731, 65

Genzel R. et al., 2006, Nat, 442, 786

Genzel R. et al., 2008, ApJ, 687, 59

Genzel R. et al., 2011, ApJ, 733, 101

Gilbank D. G., Gladders M. D., Yee H. K. C., Hsieh B. C., 2011, AJ, 141, 94

Glazebrook K., Ellis R., Santiago B., Griffiths R., 1995, MNRAS, 275, L19

Glazebrook K. et al., 2004, Nat, 430, 181

Gonçalves T. S. et al., 2010, ApJ, 724, 1373

Grandi S. A., Phillips M. M., 1979, ApJ, 232, 659

Green A. W. et al., 2010, Nat, 467, 684

Hopkins A. M., Beacom J. F., 2006, ApJ, 651, 142

Immeli A., Samland M., Gerhard O., Westera P., 2004a, A&A, 413, 547

Immeli A., Samland M., Westera P., Gerhard O., 2004b, ApJ, 611, 20

Jones T. A., Swinbank A. M., Ellis R. S., Richard J., Stark D. P., 2010, MNRAS, 404, 1247

Kauffmann G. et al., 2003, MNRAS, 346, 1055

Kennicutt R. C., Jr, 1998, ARA&A, 36, 189

Kereš D., Katz N., Weinberg D. H., Davé R., 2005, MNRAS, 363, 2

Kewley L. J., Dopita M. A., Sutherland R. S., Heisler C. A., Trevena J., 2001, ApJ, 556, 121

Komatsu E. et al., 2011, ApJS, 192, 18

Kriek M. et al., 2010, ApJ, 722, L64

Krumholz M. R., Dekel A., 2010, MNRAS, 406, 112

Larkin J. et al., 2006, New Astron. Rev., 50, 362

Law D. R., Steidel C. C., Erb D. K., Larkin J. E., Pettini M., Shapley A. E., Wright S. A., 2007, ApJ, 669, 929

Law D. R., Steidel C. C., Erb D. K., Larkin J. E., Pettini M., Shapley A. E., Wright S. A., 2009, ApJ, 697, 2057

Lemoine-Busserolle M., Lamareille F., 2010, MNRAS, 402, 2291

Lemoine-Busserolle M., Bunker A., Lamareille F., Kissler-Patig M., 2010, MNRAS, 401, 1657

Lotz J. M., Madau P., Giavalisco M., Primack J., Ferguson H. C., 2006, ApJ, 636, 592

McLean I. S. et al., 1998, in Fowler A. M., ed., Proc. SPIE Vol. 3354, Infrared Astronomical Instrumentation. SPIE, Bellingham, p. 566

Maraston C., Daddi E., Renzini A., Cimatti A., Dickinson M., Papovich C., Pasquali A., Pirzkal N., 2006, ApJ, 652, 85

Martin D. C. et al., 2005, ApJ, 619, L1

Michałowski M., Hjorth J., Watson D., 2010, A&A, 514, A67

Monet D. G. et al., 2003, AJ, 125, 984

Naab T., Burkert A., 2003, ApJ, 597, 893

Nesvadba N. P. H., Lehnert M. D., Davies R. I., Verma A., Eisenhauer F., 2008, A&A, 479, 67

Noeske K. G. et al., 2007, ApJ, 660, L43

Noguchi M., 1999, ApJ, 514, 77

Overzier R. A. et al., 2008, ApJ, 677, 37

Pettini M., Pagel B. E. J., 2004, MNRAS, 348, L59

Rodighiero G. et al., 2010, A&A, 518, L25

Rodríguez-Zaurín J., Arribas S., Monreal Ibero A., Colina L., Alonso-Herrero A., Alfonso-Garzón J., 2011, A&A, 527, A60

Sérsic J. L., 1968, Atlas de Galaxias Australes. Obser. Astron., Córdoba

Shapiro K. L. et al., 2009, ApJ, 701, 955

Shapley A. E., Coil A. L., Ma C.-P., Bundy K., 2005, ApJ, 635, 1006

Sharp R. G., Bland-Hawthorn J., 2010, ApJ, 711, 818

Sharp R. et al., 2006, in McLean I. S., Iye M., eds, Proc. SPIE Vol. 6269, Ground-based and Airborne Instrumentation for Astronomy. SPIE, Bellingham, 62690G

Skrutskie M. F. et al., 2006, AJ, 131, 1163

Springel V. et al., 2005, Nat, 435, 629

Stark D. P., Swinbank A. M., Ellis R. S., Dye S., Smail I. R., Richard J., 2008, Nat, 455, 775

Steidel C. C., Shapley A. E., Pettini M., Adelberger K. L., Erb D. K., Reddy N. A., Hunt M. P., 2004, ApJ, 604, 534

Swinbank A. M., Smail I., Chapman S. C., Blain A. W., Ivison R. J., Keel W. C., 2004, ApJ, 617, 64

Swinbank A. M. et al., 2009, MNRAS, 400, 1121

Swinbank A. M. et al., 2010, Nat, 464, 733

Tacconi L. J. et al., 2008, ApJ, 680, 246

Takata T., Sekiguchi K., Smail I., Chapman S. C., Geach J. E., Swinbank A. M., Blain A., Ivison R. J., 2006, ApJ, 651, 713

Teyssier R., Chapon D., Bournaud F., 2010, ApJ, 720, L149

Tinney C. G. et al., 2004, in Moorwood A. F. M., Iye M., eds, Proc. SPIE Vol. 5492, Ground-based Instrumentation for Astronomy. SPIE, Bellingham, p. 998

van Dam M. A. et al., 2006, PASP, 118, 310

Veilleux S., Cecil G., Bland-Hawthorn J., 2005, ARA&A, 43, 769

Wizinowich P. L. et al., 2006, PASP, 118, 297

Wright S. A. et al., 2007, ApJ, 658, 78

Wright S. A., Larkin J. E., Law D. R., Steidel C. C., Shapley A. E., Erb D. K., 2009, ApJ, 699, 421

Yuan T.-T., Kewley L. J., Swinbank A. M., Richard J., Livermore R. C., 2011, ApJ, 732, L14

APPENDIX A

A1 Multiple-emission galaxies

A1.1 WK0912_13R

WK0912_13R has an extended irregular flux profile with faint surface brightness at the centre encircled by a brighter ring of emission. This galaxy shows multiple bright regions of Hα spatial emission, however, due to low signal the individual regions are not resolved. The velocity map shows an ordered velocity gradient with the 'hole' in emission spatially placed at the central region of the velocity gradient and is well fit by a disc model. However, this detection has the lowest signal-to-noise ratio of the sample and only a portion of the rotation curve is detected. Optical emission is shown in Fig. A1.

A1.2 WK1002_61S

The morphology of 61S reflects that of 'chain galaxies' observed in the HUDF with two–three resolved clumps marked by plus signs in Fig. 3. However, unlike the clumpy galaxies 06R and 13R in this sample, 61S has one of the lowest velocity dispersions of this sample of $\sigma_{mean} = 85\,\mathrm{km\,s^{-1}}$ and shows little or no velocity separation between clumps as shown in Fig. A2. There is a messy velocity gradient across the length of the 'chain' with peaks of velocity dispersion spatially aligned with the peaks of the eastern most clumps.

A1.3 WK0909_02R

WK0909_02R has the most irregular optical morphology of the objects with available broad-band imaging. The RCS2 r-band image (0.185 arcsec pixel^{-1}) shows three distinct regions of emission spread over 4 arcsec, including the central brightest region denoted by a × in Fig. A1, a lower surface brightness feature to the northwest, and a larger low surface brightness feature to the south of the brightest region extending ~21 kpc away from the central peak of broad-band emission. The OSIRIS observations of WK0909_02R has a single peak in Hα flux with a faint tail of emission to the north-west coincident with the peak of r-band emission and faint north-west feature, respectively. [N II]λ6584 is detected with peak flux coincident with peak Hα flux. Long-slit spectroscopy with the Low Resolution Imaging Spectrometer (LRIS) reveals the southern low surface brightness component is at the same redshift as the brighter central emission.

A1.4 WK0909_06R

WK0909_06R has three resolved knots of Hα emission. In velocity space these peaks correspond to a velocity range of approximately
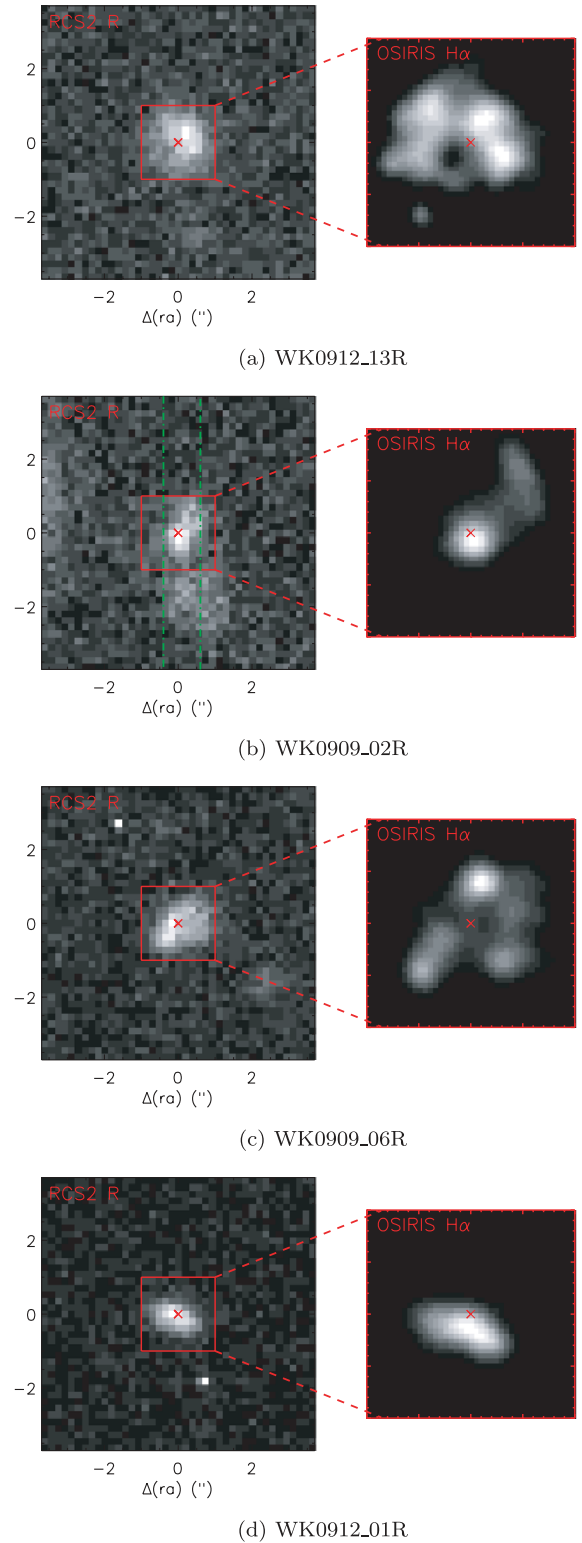

(a) WK0912_13R

(b) WK0909_02R

(c) WK0909_06R

(d) WK0912_01R

Figure A1. RCS2 r band and OSIRIS Hα images for 02R, 01R, 06R and 13R, the only objects with resolved broad-band imaging. The green dot–dash lines on the RCS2 image of 02R mark the position of the LRIS long slit. LRIS spectroscopy confirms the low surface brightness region below the central emission is at the same redshift as the central emission detected by OSIRIS.
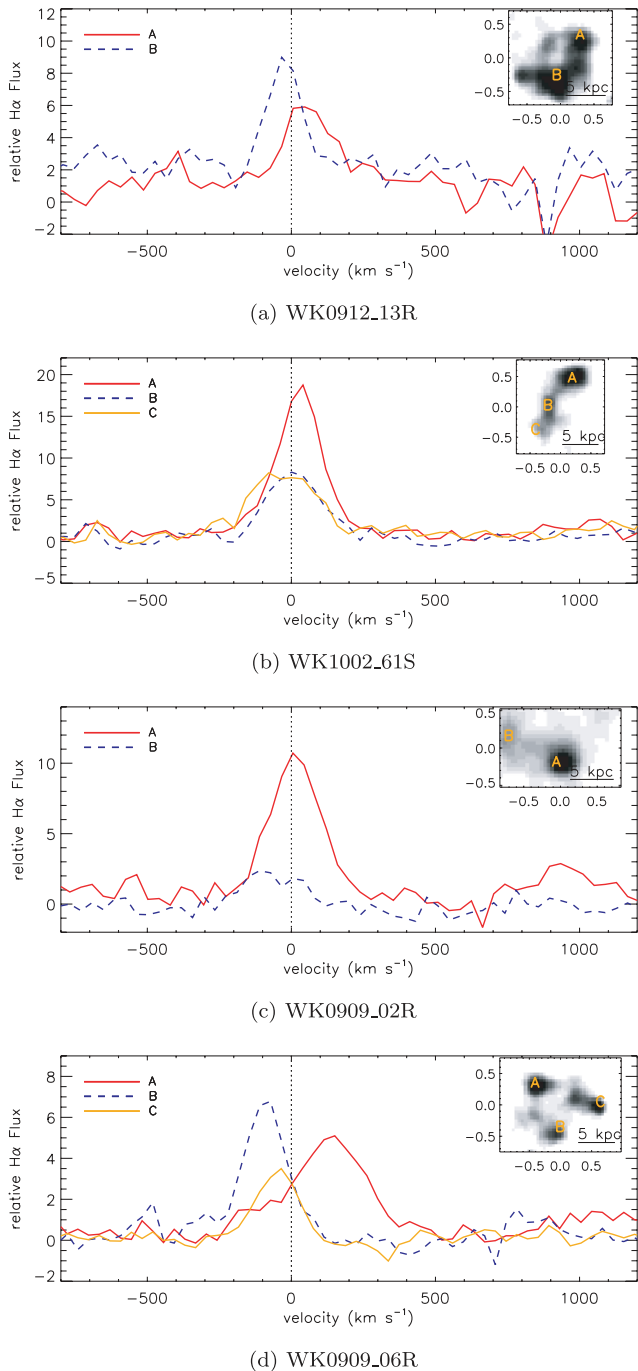
(a) WK0912_13R

(b) WK1002_61S

(c) WK0909_02R

(d) WK0909_06R

Figure A2. Integrated spectra from individual clumps for all multiple emission systems. Clumps and their corresponding spectra are labelled in Hα images found in the upper right-hand corner. The spectra are the integrated spectra of emission within $2r_{\rm eff}$ of star-forming regions that are resolved or marginally resolved.

$320\,{\rm km\,s^{-1}}$ shown in Fig. A2. This large change in velocity over $\sim 10\,{\rm kpc}$ leads to broad velocity width of the Hα emission line between flux peaks where a signature of two Gaussians is seen. Peak [N II] emission corresponds with the brightest peak of Hα and is not detected elsewhere in the galaxy. Faint [S II] emission is detected in the integrated spectrum but does not have high enough signal-to-noise ratio to be mapped spatially. The RCS2 image in Fig. A1 reveals a possible optical companion 1.8 arcsec to the south-west

(15 kpc). Future long-slit spectroscopy will determine if the galaxies are undergoing a merger.

A2 Extended-emission galaxies

A2.1 WK0905_22S

The flux profile of WK0905_22S is also best fit by two components with the primary peak of velocity dispersion occurring at the boundary of the two systems indicative of a line-of-sight merger, however, the velocity map shows evidence of rotation and is well fit by a disc.

A2.2 WK0912_01R

WK0912_01R has one extended peak of Hα flux with a fainter surrounding halo. The velocity map shows a strong velocity gradient of $v_{\rm shear} \sim 200\,{\rm km\,s^{-1}}$ and a near linear rotation curve. It is well fit by a disc with optical morphology consistent with being an edge-on system as seen by the ellipticity of the rest-frame UV image in Fig. A1. [N II] was not detected in the OSIRIS observation of this galaxy, which is partly due to its short integration time, an upper limit is given in Table 2.

A2.3 WK1002_41S

The Hα morphology of 41S reveals two peaks of emission connected by a dip in the Hα surface brightness at the central region of the detection. The rotation profile of 41S is linear ($v_{\rm shear} = 114\,{\rm km\,s^{-1}}$) with a featureless velocity dispersion; as a result there exist a strong degeneracy between $r_{\rm p}$ and $V_{\rm p}$ when fitting a disc profile. This indicates that 41S is well fit by a disc but as we only detect the inner part of rotation, the kinematic extent cannot be constrained. It follows that the dispersion map is flat and featureless as the turnover has not been reached.

A2.4 WK0809_02S

The 2D flux profile of WK0809_02S is best fit by two emission components. The peak in velocity dispersion corresponds with the brightest peak in flux, however, no clear velocity gradient is seen and the object has the lowest velocity shear in the sample ($v_{\rm shear} = 36\,{\rm km\,s^{-1}}$). With J-band photometry (K not available) the stellar mass is estimated at $\log{(M_*)} = 11.1 \pm 0.3\,{\rm M_\odot}$, one of the most massive of the sample. A tentative IRAM detection of the CO(2–1) emission line exists at $500\,{\rm km\,s^{-1}}$ from the $z_{\rm sys}$ of Hα. The CO(2–1) line is formally 2.5σ per channel, but spans >three channels, so is $\sim 5\sigma$ integrated over the line, possibly indicative of an outflow/inflow signature. This result is outside of the scope of this analysis and will be addressed in a subsequent paper.

A3 Single-emission galaxies

A3.1 WK1002_18S

WK1002_18S is a compact resolved single-emission galaxy with $n_{\rm Hα} = 0.8$ and shows a near-linear velocity gradient. The stellar mass of 18S is $8 \times 10^9\,{\rm M_\odot}$ and has a velocity dispersion $\sigma_{\rm mean} = 102\,{\rm km\,s^{-1}}$.

A3.2 WK1002_14S

WK1002_14S has a single compact region of resolved Hα emission showing a linear velocity shear, with some variations in the velocity field at the edges of the galaxy detection. As with 41S there exists a degeneracy between r_p and V_p due to the linear nature of the velocity profile. The flat dispersion map can be explained by the lack of turnover in the velocity profile. This galaxy is one of the highest dispersion galaxies with $\sigma_{mean} \sim 130\,km\,s^{-1}$ and stellar mass of $M_* = 3.7 \times 10^{10}\,M_\odot$. [N II]$\lambda$6583.5 is detected coincident with Hα emission.

A3.3 WK1002_46S

WK1002_46S is the most compact ($r_{1/2}$(Hα) $\sim 1.8\,kpc$) resolved galaxy. The stellar mass of 46S is $7 \times 10^9\,M_\odot$ and the galaxy has a relatively low $\sigma_{mean} = 85\,km\,s^{-1}$.

A3.4 WK1002_52S

52S is only marginally resolved and an outlier in many respects including highest velocity dispersion ($\sigma_{mean} = 125\,km\,s^{-1}$), highest stellar mass ($M_* = 4.6 \times 10^{11}\,M_\odot$) and most compact ($r_{1/2} \sim 1.8\,kpc$). Given the high stellar mass it is more likely that 52S is a merger remnant rather than a newly forming bulge.

A3.5 WK0912_16S

WK0912_16S is observed to have a single resolved peak in Hα flux. [N II] is detected with peak flux coincident with the peak Hα flux. 16S has one of the lowest velocity dispersions of the sample at $\sigma_{mean} \sim 90\,km\,s^{-1}$, and does not show a coherent velocity gradient. It also has the lowest stellar mass of the sample of $6.3 \times 10^9\,M_\odot$ and the flattest flux profile with $n_{H\alpha} = 0.5^{+0.3}_{-0.1}$.

This paper has been typeset from a TEX/LATEX file prepared by the author.